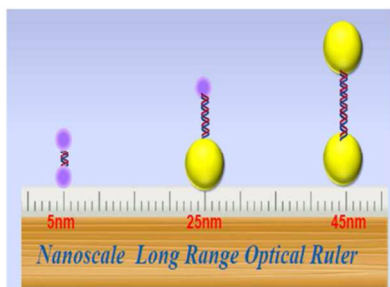




**Nanoscopic Optical Ruler Beyond FRET Distance Limit:  
Fundamentals & Applications**

Journal:	<i>Chemical Society Reviews</i>
Manuscript ID:	CS-REV-12-2013-060476.R1
Article Type:	Review Article
Date Submitted by the Author:	11-Apr-2014
Complete List of Authors:	Ray, Paresh C; Jackson State University, Chemistry & Biochemistry Fan, Zhen; Jackson State University, Chemistry Crouch, Rebecca; Jackson State University, Chemistry Sinha, Sudarson; Jackson State University, Chemistry Pramanik, Avijit; Jackson State University,

## A table of contents entry



Current review report the recent advances in the development of a long-range nanomaterials- based optical ruler.

Cite this: DOI: 10.1039/c0xx00000x

www.rsc.org/xxxxxx

REVIEW

## Nanoscopic Optical Ruler Beyond FRET Distance Limit: Fundamentals & Applications

Paresh Chandra Ray, Zhen Fan, Rebecca A. Crouch, Sudarson Sekhar Sinha, Avijit Pramanik

Received (in XXX, XXX) Xth XXXXXXXXX 20XX, Accepted Xth XXXXXXXXX 20XX

DOI: 10.1039/b000000x

Last several decades, Förster resonance energy transfer (FRET) based spectroscopy ruler served as key tool for understanding chemical and biochemical processes, even at the single molecule level. Since FRET process originates from dipole-dipole interactions, the length scale of a FRET ruler is limited to 10 nm maximum. Recently, scientist have reported a nanomaterial based long-range optical ruler, where one can overcome FRET optical ruler distance dependence limit and very useful for monitoring biological processes that occur across a greater distance than the 10-nm scale. Advancement of nanoscopic long range optical ruler in last ten years, indicate that in addition to their long-range capability, their brightness, long lifetime, non-blinking, and chemical stability make the nanoparticle based rulers a good choice for long range optical probes. Current review discuss the basic concept and unique light-focusing properties of plasmonic nanoparticles, that are useful to develop a long range one dimensional to three dimensional optical ruler. In addition, to provide the readers an over view of exciting opportunity of this field, this review discuss the applications of the longrange ruler for monitoring biological & chemical processes. At the end, we conclude by speculating about the role of longrange optical rulers in future scientific research and discuss possible problems, outlooks and future needs for using optical ruler for technological applications.

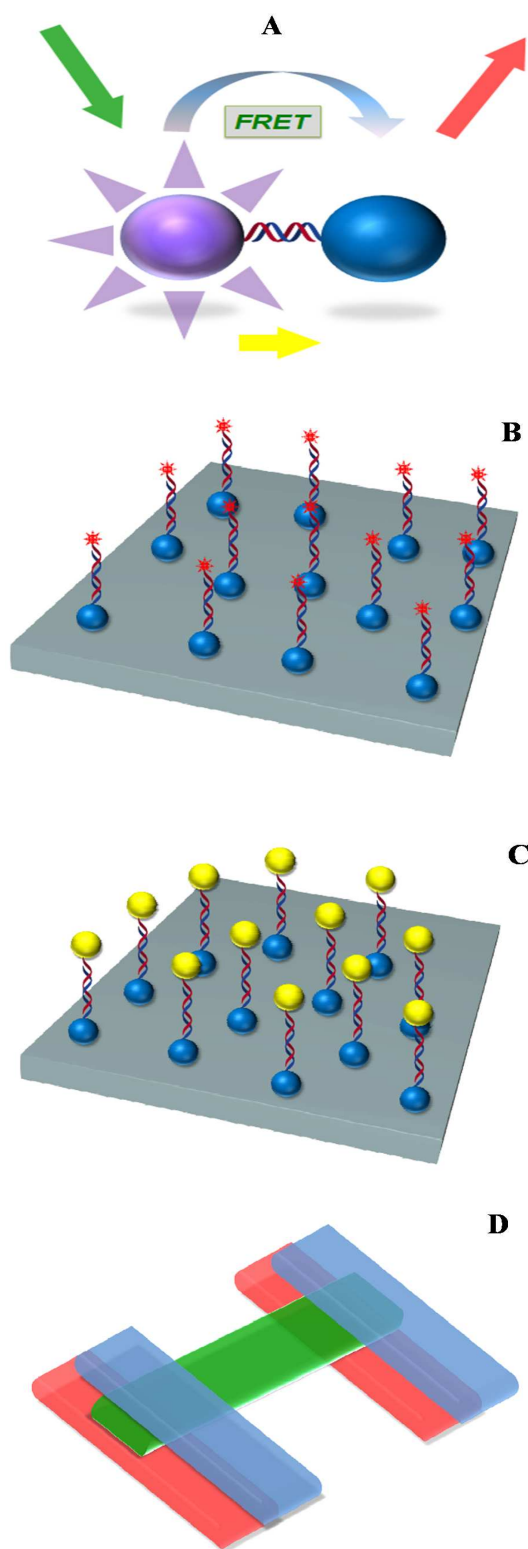
### 1. Introduction

Optical spectroscopy ruler is essential for monitoring nucleic acids, protein and other biomolecules conformational changes in drug discovery and cell biology.<sup>1-5</sup> It is the key tool for understanding biochemical processes, and it has been used in a wide range of applications in analytical biochemistry.<sup>6-15</sup> In 1967, Stryer and Haugland introduced for the first time, Förster resonance energy transfer (FRET) as a “spectroscopic ruler”, for the distance measurement in biological process.<sup>2</sup> According to the quantum physical model and the classical Coulombic dipole-dipole interactions, FRET occurs via radiationless transitions.<sup>16-23</sup> The energy transfer efficiency depends highly on the relative distance between the FRET pair.<sup>24-27</sup> After Stryer’s and Haugland’s report,<sup>2</sup> the FRET optical ruler opened a new window to use molecular rulers to address a wide range of biological activity, which is now applicable for obtaining distance information on the single biomolecule level.<sup>4-10</sup>

FRET rulers have been used in biological and chemical systems to determine distances on the molecular scale and as instruments for following the dynamics of attachment processes and changes in configurations and dimensionality of systems.<sup>11-17</sup> Over the past few decades, single-molecule FRET has become a sensitive and powerful tool for determining conformational biomolecular changes and molecular interactions and it has been used for inter- and intramolecular distances measurement for biochemical processes.<sup>15-20</sup> After FRET has been introduced in light microscopy imaging, huge interest has been generated in obtaining spatial and temporal distribution of protein and DNA/RNA associations in living cells.<sup>22-27</sup>

Since FRET process originates from dipole-dipole interactions, the energy transfer between donor and acceptor, is strongly depend on the center-to-center separation distance, as shown in Scheme 1A. Due to the coupling requirement, the energy transfer efficiency is inversely proportional to the sixth power of the donor to acceptor distance.<sup>2-3</sup> As a result, the length scale of a FRET ruler is on the order of 10 nm maximum. This fact prompted scientists to develop a long-range optical ruler, which would be useful for monitoring biological processes that occur across a greater distance than the 10-nm scale.<sup>28-29</sup> Recently, we and other groups have reported a long-range plasmonic nanoparticle-based surface energy transfer (NSET) and a surface-enhanced Raman spectroscopy (SERS) ruler, where one can overcome FRET optical ruler distance dependence limit,<sup>30-50</sup> as shown in Scheme 1. If the distance  $R$  between the donor & acceptor is not too small, the transfer occurs due to the coulomb interaction. On the other hand, when the distance between dye donor and metal nanoparticle acceptor is high, the matrix element for the energy transfer depends on the transition dipoles of the two dyes. Since in case metal nanoparticle, metals have a continuum of electron-hole pair excitations, the density of these excitations is proportional to the excitation energy. Experimentally, several groups including ours found an  $R^{-4}$  dependence of the rate of energy transfer from the oscillating dipole to the continuum of electron-hole pair excitations in a metal.<sup>51-70</sup> In this review, we discuss recent advances in the development of a long-range nanomaterials- based optical ruler. We also discuss the development of long-range optical ruler and its applications in biology, medicine, and materials science. Finally, we conclude by speculating about future research directions and possible several challenges in technological applications of optical rulers.

<sup>a</sup> Department of Chemistry and Biochemistry, Jackson State University, Jackson, MS, USA; E-mail:paresh.c.ray@jsums.edu; Fax:+16019793674.



**Scheme 1:** Schematic representation of different type of optical rulers, discussed in this review article. A) Schematic representation of a short-range FRET ruler, where a pair of organic dyes act as a donor and an acceptor. B) Schematic representation of a long-range NSET ruler, where organic dye acts as donor and nanoparticle acts as acceptor. C) Schematic representation of a long-range plasmon ruler consisting of two

nanoparticles. D) Schematic diagram of a long-range 3D plasmon ruler consisting of two pairs of metal nanorods and a central dipole antenna.

## 2. Scope of This Review

We begin with a historical account showing the evolution of the FRET optical ruler<sup>4-27</sup>. This allows us to acknowledge contributions of great scientists on the development of the FRET optical ruler. Next we discuss the long-range plasmon ruler. In the last decade, different types of plasmon rulers have been developed, as shown in Scheme 1C-1D. It has also been demonstrated that plasmon rulers can be used to determine nanoscale distances within chemical or biological species<sup>29-35</sup>. Plasmon arises in nanoparticles due to the collective oscillation of the free electrons within a metal nanoparticle<sup>36-44</sup>. It is now well-documented<sup>45-43</sup> that when two nanoparticles are brought into close proximity (within  $\sim 2.5$  times the particle diameter) there is an interaction between the localized surface plasmons that is mediated by their electric fields, resulting in a Coulomb-like coupling between them. Since the spatial variation of the electric field gives rise to a spatial dependence of the interaction, optical resonances depend on the distance between the nanoparticles, which has been exploited in creating the plasmonic ruler<sup>54-63</sup>. The simplest description of two interactions in the plasmon ruler is in the coupling of two nearby dipoles. The interaction energy is sufficiently strong in the case of nearly-adjacent metallic nanoparticles, resulting in the new red-shifted and blue-shifted resonances relative to the resonance of each individual nanoparticle<sup>64-73</sup>. In the case of metallic spheres, the lower-energy resonance corresponds to two longitudinally aligned dipoles, giving rise to the strong red-shifted absorption peak in the optical spectrum. On the other hand, in the case of higher energy resonance, the coupled dipoles cancel each other, resulting in a resonance with essentially a zero net dipole moment<sup>74-83</sup>. Higher order multipoles can also contribute to this interaction, depending on nanoparticle size.

Several groups have demonstrated that plasmon rulers can be used to probe the structural dynamics of complex macromolecular processes<sup>29,32-38,40,67</sup>, where the conformation of the molecules and their variation with time are important. It has been reported that the plasmon ruler is effective in measuring distances over the 1- to 100-nm range, which makes it a unique tool for studying macromolecular assemblies and conformational changes at the single-molecule level<sup>29,32-38,67</sup>. In 2011, the plasmon ruler idea was extended to three dimensions using gold nanorod which are sensitive to both separation and translation<sup>67</sup>. The reported 3D plasmonic ruler exhibits the presence of two sub-radiative plasmonic resonances excited by near-field coupling to a plasmonic dipole antenna, as shown in Scheme 1D. In this review, we discuss the unique light-focusing properties of strongly-coupled plasmonic systems, which help to develop a long range 1D-3D plasmon ruler. We also describe a theoretical picture of plasmon hybridization for intuitive explanation of the properties of complex plasmonic systems. Additionally, we examine a broad range of metal nanoparticles with different sizes and shapes that give rise to strong plasmon coupling, as well as how plasmon ruler distance varies with size and shape of nanoparticles. Finally, we will discuss applications of the long-range plasmon ruler for biological and chemical activities.

In the last decade, several reports demonstrated that gold nanoparticles can be used as very highly efficient energy acceptors to substitute for FRET acceptors<sup>84-90</sup>. When an

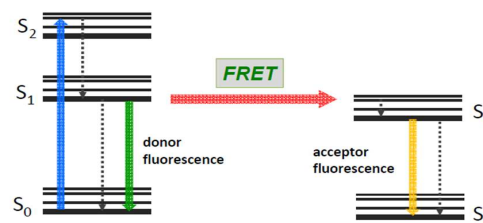
acceptor nanoparticle and a donor organic dye are brought into proximity, there is a dipole-surface type energy transfer from dye molecule dipole to nanometal surface, which can be termed as nanoparticle based surface energy transfer (NSET)<sup>91-98</sup>, as shown in Scheme 1B. NSET is a through-space mechanism like FRET, and it arises from the damping of the fluorophore's oscillating dipole by the gold metal's free electrons<sup>99-108</sup>. Like FRET, the interaction for NSET is dipole-dipole in nature but is geometrically different because an acceptor nanoparticle has a surface and an isotropic distribution of dipole vectors to accept energy from the donor<sup>109-120</sup>. This arrangement increases the probability of energy transfer and accounts for the enhanced efficiency of NSET over FRET<sup>121-128</sup>. In the case of resonant surface-plasmon excitation, a small dipole in the excited fluorophore induces a large dipole in the particle, leading to an enhancement in the energy-transfer efficiencies<sup>129-136</sup>. Several experimental observations reports the design of optical-based molecular ruler strategies that can be used at distances more than double those achievable using traditional dipole-dipole Coulombic energy transfer based methods<sup>137-150</sup>. We and other groups have demonstrated applications of NSET optical molecular rulers to address questions in biochemistry, bio-diagnostics, and biomolecular imaging<sup>150-160</sup>. We and others have shown that NSET rulers could be useful for monitoring structural changes in biological samples, such as RNA folding and DNA interactions, etc.<sup>29,96-97,100-106,125-129</sup>. In this review, we first discuss the development of NSET rulers, using a nanoparticle-dye pair or a pair of different nanoparticles. We explain how the size and the shape of the nanoparticle are important in varying the NSET ruler length. Considering the importance of theory in understanding long-distance ruler working principles, we also provide the reported theoretical background. Finally, we review the applications of the long-range NSET ruler for monitoring biological & chemical dynamics.

The possibility of observing very weak normal Raman signals, with enhancements on the order of  $10^6$ - $10^{14}$  in the presence of a metal nanomaterial surface<sup>181-190</sup>, allow surface-enhanced Raman spectroscopy (SERS) to be very attractive for ultrasensitive biological and chemical analysis<sup>191-208</sup>. As a result, a long-range SERS ruler would be very useful for monitoring biological processes at very low concentrations<sup>162-164</sup>. Recently, we and another group have shown that one can tune the SERS ruler length to about 20 nm by choosing the size and shape of the nanoparticle<sup>162-164</sup>. In this current review, we highlight the recent advancements in the development of a long-range SERS ruler and its use for monitoring biological processes. We discuss about the role of long-range optical rulers in future scientific research and technological applications. We also discuss future research directions to overcome possible toxicity problems.

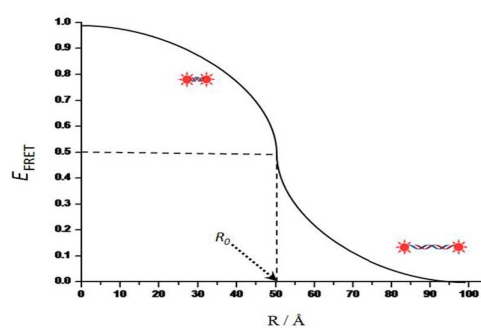
### 3. Short-Range FRET Optical Ruler

In 1949, Theodor Förster reported the theoretical basis of an energy transfer mechanism<sup>1</sup>. In his model, Förster assumed that the oscillating dipole moments are identical and the interaction energy is small compared to the energies of the spectral transitions<sup>2-10</sup>. The working principle behind FRET involves the radiationless energy transfer process in which an energetically-excited donor fluorophore transfers energy to another dye molecule. The second dye molecule acts as an acceptor, and energy transfer occurs via a dipole-dipole through-space mechanism<sup>11-20</sup>. In the end, the excited acceptor molecule returns to the ground state by losing its energy via photon emission<sup>21-27</sup>,

as shown in Scheme 2. If the distance  $R$  between the donor and acceptor dye is not too small, the transfer occurs due to the Coulomb interaction. For a large enough  $R$ , the matrix element for the transfer reduces to an interaction between the transition-dipoles of the two dyes and has  $R^{-3}$  dependence, and hence the rate behaves like  $R^{-6}$ .



**Scheme 2:** Schematic representation showing the energy transfer from excited donor to acceptor via a non-radiative process, which is known as FRET.



**Scheme 3:** Demonstrating how FRET efficiency depends on the distance between the FRET pair ( $R$ ).

FRET can be used for the weak coupling limit because it is based on an equilibrium Fermi Golden Rule approach<sup>15-23</sup>. The key assumptions for the FRET process are the following: 1) The bath equilibrates subsequent to electronic excitation of the donor on a timescale that is considerably faster than that of resonance energy transfer<sup>4-9</sup> and 2) the coupling to the bath is much greater than the electronic coupling between donor and acceptor<sup>10-15</sup>. As conferred in the Equation 1-4, the FRET efficiency varies with the sixth power of the distance between the two molecules ( $R$ ) and can be determined using the following equations<sup>3-12</sup>:

$$k_{\text{FRET}} = \frac{1}{\tau_0} \left( \frac{R_0}{R} \right)^6 \quad (1)$$

$$R_0^6 = 8.79 \times 10^{23} \frac{\kappa^2 \Phi_D J}{n^4} \quad (2)$$

$$\kappa^2 = (\cos \theta_T - 3 \cos \theta_D \cos \theta_A)^2 \quad (3)$$

$$J = \int_0^\infty f_D(\lambda) \epsilon_A(\lambda) \lambda^4 d\lambda \quad (4)$$

where  $R_0$  is the characteristic distance at a FRET efficiency of 50%, which varies for different FRET pairs and also with their orientation. FRET efficiency depends on  $\tau_0$ , which is the donor fluorescence lifetime in the absence of acceptor.  $R_0$  is proportional to the orientation factor  $\kappa$ , the donor-acceptor spectral overlap  $J$ , and the donor quantum yield  $\Phi_D$ . As shown in equations 2-4, usually  $\kappa^2$  depends on  $\theta_T$ ,  $\theta_D$  and  $\theta_A$  values.  $\theta_T$  is the angle between the donor emission dipole and the acceptor absorption dipole.  $\theta_D$  is the angle between the donor-acceptor

connection line and the donor emission dipole. Similarly  $\theta_A$  is the angle between the donor-acceptor connection line and the transition dipole moment of the acceptor. The spectral overlap integral  $J$  involves the normalized fluorescence emission spectrum of the donor  $f_D$  and the molar extinction coefficient of the acceptor  $\epsilon_A$ . For distances close to  $R_0$ , FRET can be employed as a molecular ruler due to higher precision in the measurement<sup>3-15</sup>. The advantage of the FRET technique is that it allows measurement of the internal distance in the molecular frame rather than in the laboratory frame, which makes it largely immune to instrumental noise and drift<sup>16-25</sup>. Spectacular progress has been made in the last two decades in the field of FRET design to answer biological questions<sup>4-20</sup>. After Taekjip et al.,<sup>4</sup> reported on the visibility of single molecular FRET, it has been developed rapidly by several groups to answer fundamental natural questions in biology, regarding replication, recombination, transcription, translation, RNA and protein folding and conformational changes, ion channels, and signal transduction<sup>5-25</sup>. These are just a few examples, and the list keeps growing every year. Since the goal of this review is to discuss the long-range optical ruler, we refer the reader to the literature to review FRET<sup>17,20-27</sup>.

FRET has been advanced into an elementary tool for characterizing proteins, signaling pathways and many other biological phenomenon in last two decades<sup>17,20-27</sup>. As we discussed before, FRET has the limitation as a molecular ruler for the study of biological processes only in the range of 2–10 nm. Due to the distance limitation, normal FRET optical rulers are not suitable for the investigation of the structural change phenomena for biological systems where the donor and acceptor distances are >10 nm. Also, photo-bleaching of the organic donor-acceptor dyes limits the maximum duration of single-molecule trajectories. The blinking of the dyes complicates the decomposition of single-molecule FRET traces into molecular trajectories and states<sup>17,20-27</sup>. This fact has driven scientists to develop the long-range optical ruler, which will be useful for monitoring biological processes happening outside the 10-nm scale. In the next section, we discuss recent developments of different types of long-range optical rulers.

#### 4. Long-Range Nanomaterial-Based Optical Ruler

Optical ruler that does not alter the biomolecular function and is able to investigate long range dynamical process, is very important to understand complicated dynamics of biological important molecules. Recently, several groups including ours have reported that the limitations of the FRET optical ruler can be overcome with a long-range plasmonic, nanoparticle based surface energy transfer (NSET) and surface enhanced Raman spectroscopy (SERS) ruler. Optical properties of metal nanoparticles are controlled by their plasmons, which are collective oscillations of their conduction electrons. Outstanding optical properties of metallic nanoparticles were exploited in the colorful stained glass windows of medieval Europe for several centuries, even before the modern science provided an understanding of their origin. In the past twenty years, as the fundamentals of nanoscience have gained enormous interest, we realized that the surface plasmon properties are also largely controlled by the shape and size of the metal structure at sub-wavelength dimensions<sup>28-40</sup>. With the advances of plasmonic nanoscience, we now understand that plasmonic properties can be designed by the selection and fabrication of metallic structures of specific geometries<sup>37-45</sup>. Due to the advancement of the synthetic

protocol, the plasmon wavelength can be tuned from blue to infrared by manipulating metal nanoparticles shape and structure<sup>46-57</sup>. Plasmonic properties of metal nanoparticles are also highly sensitive to the proximity of other metal nanoparticles, because plasmons couple in a distance-dependent matter<sup>58-67</sup>. As the interparticle distance decreases, the plasmon resonance wavelength red-shifts and the scattering cross-section increase. Such distance dependent properties have been exploited to design long-range plasmon ruler<sup>29,46-56</sup>. Recent reports show that the individual pairs of double-stranded DNA-linked noble metal nanoparticles can be developed to act as dynamic molecular rulers for distances in the 1-70 nm range<sup>29,38-44</sup>. In addition to their long-range capability, their brightness, long lifetime, non-blinking, and chemical stability make the nanoparticle based rulers a good choice for long-range optical probes<sup>29,38-48</sup>. Now, I will discuss nanomaterial based plasmon ruler.

#### 5. Long-Range Plasmon Ruler via Plasmon Coupling

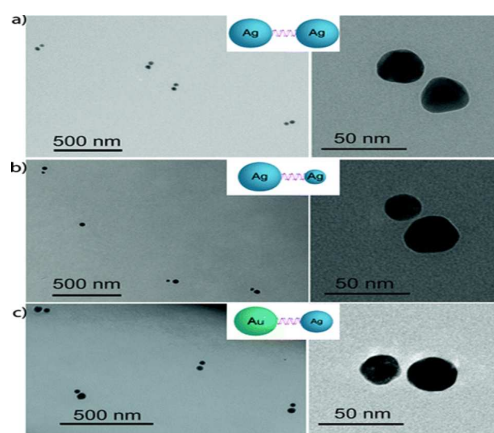


**Figure 1:** Low- (left) and high- (right) magnification transmission electron microscope images of nanoparticle dimers. (a) Symmetric dimers composed of 40 nm silver nanoparticles, (b) asymmetric dimers composed of a 20 and a 40 nm silver nanoparticle, and (c) asymmetric dimers composed of a 30 nm silver nanoparticle and 40 nm gold nanoparticle. Reprinted with kind permission from reference 54, copyright 2010, American Chemical Society.

As stated earlier, the fundamental principle of plasmon rulers is based on the distance dependence of the plasmon coupling between individual pairs of metal nanoparticles to measure distance changes<sup>28-40</sup>. When nanoparticles are placed close to each other, due to their plasmon coupling, the plasmon resonance shifts, as shown in Figures 1-3. As a result, a strong squeezing of light in the gap region occurs. Much experimental and theoretical data have reported huge local electric field enhancements due to the placement of two metal nanocrystals in close packing<sup>54</sup>, as shown in Figures 1-3. Strong interaction between nearly adjacent gold or silver nanoparticles results in new red-shifted and blue-shifted resonances relative to the resonance of each individual nanoparticle<sup>54</sup>. The lower-energy resonance is believed to be due to two longitudinally aligned dipoles, which allow for the strong red-shifted absorption peak in the optical spectrum<sup>54</sup>. In the case of the higher energy resonance, the coupled dipoles cancel each other out, which results in a resonance with essentially a zero net dipole moment. As a result, it does not interact with incident light and does not appear in the optical absorption of the homodimers. Pioneering work by the Nordlander and Halas, El-Sayed and

Alivisato's groups<sup>29,44-46,51</sup> reported that the plasmon coupling between two nanoparticles could be understood as analogous to molecular hybridization.

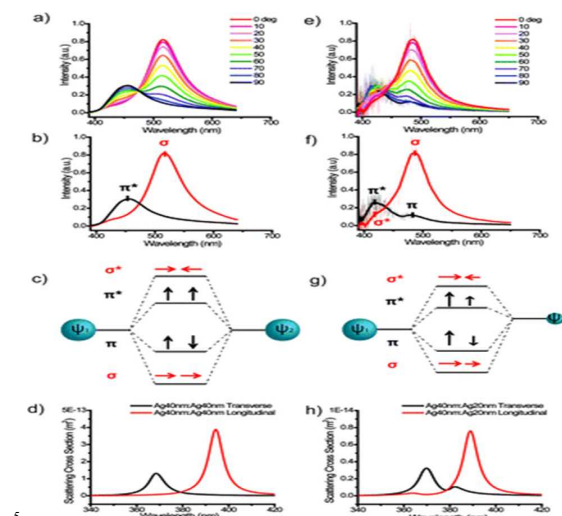


**Figure 2:** Plasmon coupling of symmetric (a–d) and size-asymmetric (e–h) silver nanoparticle dimers. Scattering spectra from a symmetric (a) and an asymmetric (e) dimer as a function of the polarizer angle (0–90°). Two extreme cases from the polarization experiments of the symmetric and the asymmetric dimers are presented in panels (b) and (f), respectively. These match well with the hybridization model (c, g) and with the scattering spectra predicted using a coupled dipole–dipole model in the quasistatic approximation (d, h). Reprinted with kind permission from reference 54, copyright 2010, American Chemical Society.

As discussed in Figures 2-3, if the plasmon modes are  $\Psi_1$  and  $\Psi_2$  for two interacting metal nanoparticles, after hybridization, they will be either in-phase ( $\Psi_1 + \Psi_2$ ) or out-of-phase ( $\Psi_1 - \Psi_2$ ). In the presence of incident light, which is polarized along the interparticle-axis, the in-phase combination will reflect a bonding mode, where the electric field is enhanced at the junction and a plasmon frequency is shifted to the red<sup>54</sup>. On the other hand, the out-of-phase mode represents an antibonding configuration, where the electric field localized on the nonjunction ends of the particles results in a blue-shifted plasmon frequency. These in-phase and out-of-phase states have been denoted as  $\sigma$  and  $\sigma^*$  in the Figures 2-3. In the other scenario, when the polarization is perpendicular to the interparticle axis, the behavior will be exactly reversed. As a result, in-phase combination is an antibonding mode, termed  $\pi^*$ . On the other hand, the out-of-phase one is a bonding mode, termed  $\pi$ , as shown in Figures 2-3. As we have discussed before, in the case of plasmonic “homodimers”, the antiphase mode is spectrally dark due to the cancellation of the equal but oppositely oriented dipoles on the two particles. As shown in Figures 2 & 3, a homodimer structure under longitudinal polarization supports only a bonding plasmon mode with its electric field strongly localized at the junction of the dimer. On the other hand, only a  $\pi^*$ -mode is observed in a homodimer under transverse polarization. Usually, heterodimers exhibit more complex plasmon coupling behaviors than homodimers. This is due to the symmetry breaking in the heterodimers, which leads to the formation of new plasmon modes, as shown in Figures 2-4. Strong interactions between different plasmon modes (broad super-radiant “bright” modes and narrow sub-radiant “dark” modes) arise. Both these modes can be responsible for the Fano resonance in asymmetric plasmonic nanostructures<sup>47</sup>.

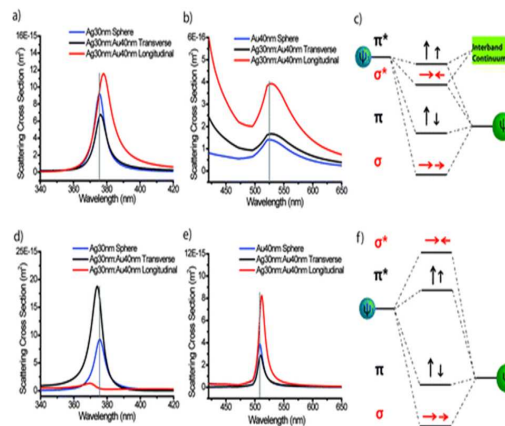


**Figure 3:** Interband absorption contribution of gold to the coupling in a silver/gold heterodimer. The coupled dipole–dipole model using the full dielectric function shows red shift of the high-energy modes ( $\pi^*$  at 376 nm and  $\sigma^*$  at 378 nm) with respect to the isolated silver nanoparticle mode (at 375.5 nm) (a) in addition to the red shift of low-energy modes ( $\pi$  at 528 nm and  $\sigma$  at 529 nm) with respect to the gold nanoparticle mode (centered at 525 nm) (b). Modified hybridization model incorporating the interband contribution is depicted in panel (c). In contrast, calculations using a dielectric function with imaginary part of the interband absorption of gold removed exhibit red shifts of the low-energy modes ( $\pi$  at 509.5 nm and  $\sigma$  at 512 nm) with respect to the gold nanoparticle mode (at 508.5 nm) (e) but blue shifts of the high-energy modes ( $\pi^*$  at 374 nm and  $\sigma^*$  at 369.5 nm) with respect to the isolated silver nanoparticle mode (at 375.5 nm) (d), as would be expected from the plasmon hybridization model (f). Reprinted with kind permission from reference 54, copyright 2010, American Chemical Society.

As shown in Figure 4, in the presence of Fano resonance, an asymmetrical Fano profile with a clear Fano minimum, due to destructive interference, appears in the spectral responses. As shown in Figure 4, Brown et al.,<sup>47</sup> have shown that in the case of heterodimer structures, avoided crossing behavior, Fano resonances, and asymmetric scattering are quite common.

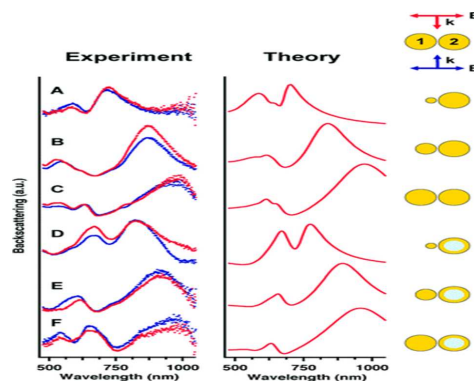


**Figure 4:** Experimental and theoretical scattering spectra for heterodimers A–F with longitudinally polarized incident light. Because the spectra for opposing  $k$ -vectors are identical due to symmetry, theoretical spectra include only one direction of propagation. Reprinted with kind permission from reference 47, copyright 2010, American Chemical Society.

## 5.1. 2D Plasmon Ruler

By using the LSPR coupling behavior with separation distance between nanoparticles, a plasmon ruler can be developed with long range capability. As we have discussed before, FRET quenching has a  $1/R^6$  dependence on the separation distance,

whereas the distance dependence of plasmonic coupling occurs as  $1/R^3$ , which allows the long-range measurement capability for the plasmon ruler, on the order of 1–100 nm. Several experimental data show that the controlled separation of two nanomaterials can be achieved in solution by using conjugated double-stranded (ds) DNA. Accurate control over the nanomaterial separation distance can be obtained by conjugating one nanoparticle with single-stranded (ss) DNA and conjugating a second nanoparticle with the complementary ss-DNA. After that, when two ss-DNA conjugated nanoparticles are mixed, due to the DNA hybridization, a rigid molecular spacer between two nanospheres of a well-defined length are formed. By changing the ss-DNA length, one can vary the ruler length. In 2011, this distance dependent coupling idea was extended to three dimensional (3D) plasmon ruler using a more complex nanoparticle structure, where the plasmon ruler is sensitive to both separation and translation<sup>67</sup>. In the case of the designed 3D plasmon ruler, the nonradiative resonances were fashioned by the interaction between pairs of metal nanorods which lead to a quadrupole resonance with very low scattering. Energy from the dipole antenna couples into the quadrupole mode, which results in a drop in the overall scattered intensity<sup>67</sup>.

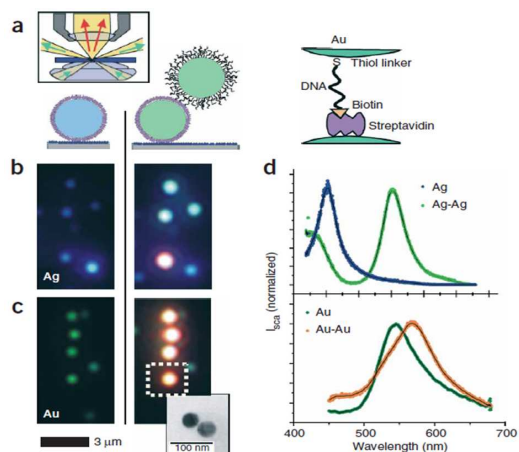


**Figure 5:** Color effects on directed assembly of DNA-functionalized gold and silver nanoparticles. (a) First, nanoparticles functionalized with streptavidin are attached to a glass surface coated with BSA-biotin (left). Then, a second particle is attached to the first particle (center), again via biotin-streptavidin binding (right). The biotin on the second particle is covalently linked to the 3' end of a 33 base pair-long ss-DNA bound to the particle via a thiol group at the 5' end. Inset: principle of transmission darkfield microscopy. (b) Single silver particles appear blue (left) and particle pairs blue-green (right). The orange dot in the bottom comes from an aggregate of more than two particles. (c) Single gold particles appear green (left), gold particle pairs orange (right). Inset: representative transmission electron microscopy image of a particle pair to show that each colored dot comes from light scattered from two closely lying particles, which cannot be separated optically. (d) Representative scattering spectra of single particles and particle pairs for silver (top) and gold (bottom). Silver particles show a larger spectral shift ( $10^2$  nm) than gold particles (23 nm), stronger light scattering and a smaller plasmon line width. Gold, however, is chemically more stable and is more easily conjugated to biomolecules via  $-SH$ ,  $-NH_2$  or  $-CN$  functional groups. Reprinted with kind permission from Reference 29. Copyright 2005 Nature Publishing Group.

Sönnichsen *et al.* demonstrated for the first time in 2005 that plasmon coupling can be used to monitor distances between single pairs of gold and silver nanoparticles<sup>29</sup>. In their experiment, 40 nm sized gold and silver nanoparticles were used. To design a plasmon ruler, at first, nanoparticles were

functionalized with streptavidin which were attached to the glass surface coated with BSA-biotin, as shown in Figure 5. After that, a second particle was attached to the first particle by a 33 base pair-long ssDNA bound to the particle via a thiol group. Nanoparticles were illuminated with unpolarized white light. After that, the scattered light by individual particles was collected using a darkfield microscope in transmission mode. As shown in Figure 5, upon illumination, nanoparticles were vividly colored. Individual silver nanoparticles were blue, and gold nanoparticles were green. It is interesting to view in Figure 5 that, after the formation of nanoparticle pairs via ssDNA, a nice change in color due to dimer formation was observed. Silver particles turned from blue to green, and gold particles turned from green to orange. It was also shown that no color change was observed in a control experiment with particles lacking biotin. The two-particle complexes were stable and could be continuously monitored for hours. Their experimental data demonstrated that plasmon rulers have the potential to become an alternative to FRET in single-molecule experiments, especially for applications demanding long observation times.

In the same year, 2005, Reihnard *et al.*, reported development of plasmon rulers using pairs of noble metal nanoparticles, and they have shown that these can be used to measure distances via the distance dependence of their plasmon coupling behavior<sup>51</sup>. They have assembled dimers using dsDNA with various interparticle spacings. They have used dsDNA spacers of 10, 20, 40, 67, 110, and 250 base pairs modified with biotin and digoxigenin at opposing ends to assemble dimers of antidigoxigenin and surface-immobilized neutravidin-coated gold nanoparticles. After designing the ruler, they measured their plasmon resonance wavelength using a darkfield microscope with unpolarized white light. To measure the distance between two nanoparticles in the plasmon ruler, the end-to-end distance of the DNA was obtained using a persistence length of 53 nm and a contour length per basepair of 0.34 nm. The thickness of the protein layer was measured by dynamic light scattering to be  $\sim 4$  nm. As shown in Figure 6, the plasmon resonance distributions show a blueshift with increasing interparticle distance. It is also interesting to note that the distributions for the 87-nm plasmon rulers are consistently broader than those for the 42-nm particles. As shown in the Figure 6, their results demonstrated that the plasmon ruler can easily be designed to measure distances between 1 and 80 nm with a time resolution  $< 50$  ms using 80 nm particles, which is significantly larger than FRET distance.

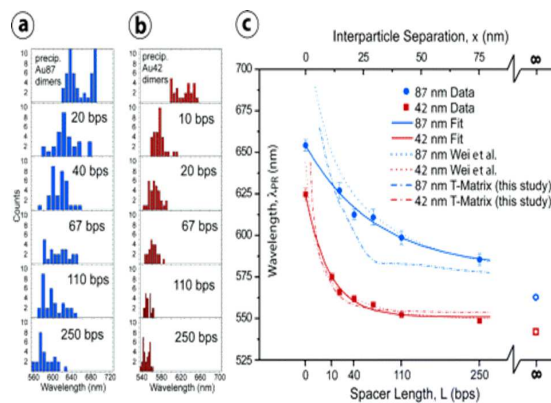


**Figure 6:** Plasmon resonance vs interparticle separation: Distributions of measured plasmon resonance wavelengths for selected dsDNA spacer lengths for (a) 87-nm Au plasmon rulers and (b) 42-nm Au plasmon rulers. Included are data points for salt-precipitated dimers at  $x = 0$ . (c)

Plot of the average plasmon resonance as a function of spacer length,  $L$ , (bottom axis) and approximated interparticle distance  $x$  (top axis) for 42-nm (red squares) and 87-nm (blue circles) plasmon rulers. The plasmon resonance wavelengths for dimers with infinite separations (=monomers) are included as open symbols. The reported errors are the standard errors of the mean. The continuous lines show fits (single exponentials  $y(x) = A_0 \cdot \exp(-x/D_0) + C$ ) to the experimental data. Best-fit parameters for 42-nm Au particles:  $C = 550.87$  nm,  $A_0 = 73.48$  nm,  $D_0 = 10.24$  nm; for 87-nm Au particles:  $C = 579.66$  nm,  $A_0 = 74.42$  nm,  $D_0 = 30.23$  nm. The dotted lines represent T-matrix simulations by assuming illumination with light polarized along the interparticle axis, and dot-dashed lines are T-matrix simulations assuming nonpolarized illumination. Reprinted with kind permission from reference 51. Copyright 2005, American Chemical Society.

Jain *et al.* reported localized surface plasmon resonances in lithographically-fabricated gold nanodisc pairs using microabsorption spectroscopy<sup>46</sup>. As shown in Figure 7A & 7B, their experimental data shows that interparticle plasmon coupling strength for polarization along interparticle axis decays nearly exponentially with a decay length of roughly 0.2 in units of the particle size for different nanoparticle. They have also used the discrete dipole approximation (DDA) method to simulate the LSPR spectra of the Au nanodisc pairs. They have derived the “plasmon ruler equation” for a Au particle pair as:

$$\frac{\Delta\lambda}{\lambda_0} \approx 0.18 \exp\left(\frac{-s/D}{0.23}\right) \quad (5)$$

where  $\Delta\lambda/\lambda_0$  is the fractional plasmon shift,  $s$  is the interparticle edge-to-edge separation, and  $D$  is the particle diameter. Their reported results show that universal plasmon scaling behavior can be a useful guide for the design of nanostructured devices, which are based on interparticle plasmon coupling, especially the plasmon ruler. As shown in Figure 7B, their experimental and theoretical data show that the plasmon coupling strength has a softer dependence on the particle separation, which is  $1/R^3$  within dipole approximation. As a result, it provides a much longer interaction range as compared to FRET, which has  $1/R^6$  dependence. They have also demonstrated that the particle size can be employed as a direct handle for increasing the ruler range, irrespective of the effect of nanoparticle shape, metal type, or medium dielectric constant.

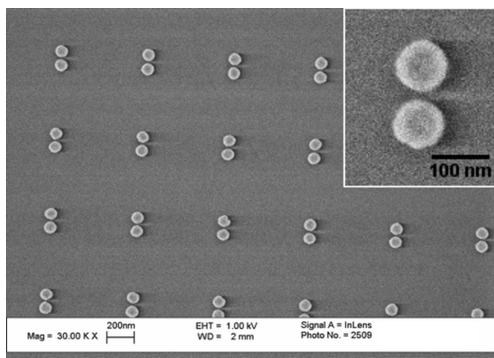


**Figure 7A:** Representative SEM image of the array of nanodisc pairs used in the present study, having an interparticle edge-to-edge separation gap of 12 nm, showing the homogeneity of the sample. The inset shows a magnified image of a single nanodisc pair, clearly showing the interparticle gap. Each nanodisc has a diameter of 88 nm and thickness of 25 nm. Images of arrays with other interparticle gaps are not shown. Reprinted with kind permission from reference 46. Copyright 2007, American Chemical Society.

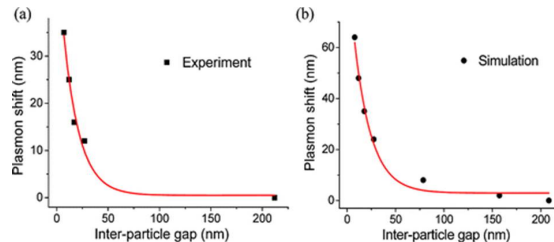


**Figure 7B:** Shift in the plasmon wavelength maximum of a pair of Au nanodiscs as a function of the interparticle edge-to-edge separation gap for (a) experiment and (b) DDA simulation. The red curves are least-squares fits to single-exponential decay  $y = y_0 + a \cdot e^{-x/l}$ , yielding a decay length  $l$  of  $15.5 \pm 3.0$  nm ( $R^2 = 0.985$ ) for experiment and  $17.6 \pm 2.5$  nm ( $R^2 = 0.989$ ) for simulations. Reprinted with kind permission from reference 46. Copyright 2007, American Chemical Society.

Ben *et al.*, reported a systematic study of the validity of the universal plasmon ruler equation in the case of periodic 2D arrays of gold nanospheres with diameters ranging from 20 to 100 nm<sup>48-49</sup>. As shown in Figures 8, their result indicates that for nanosphere diameters smaller than about 70 nm, the nanodisc dimers’ plasmonic behavior follows the universal plasmon ruler equation. On the other hand, for 2D arrays with nanosphere diameters larger than about 70 nm, a clear deviation from the universal plasmon ruler behavior has been observed. Their data reported a decrease in extinction efficiency with decreasing gap distance. Their theoretical results show that the anomalous size-dependent optical responses can be interpreted by including dynamic depolarization effects within a semi-analytical coupled dipole approximation, which accounts for structural retardation.

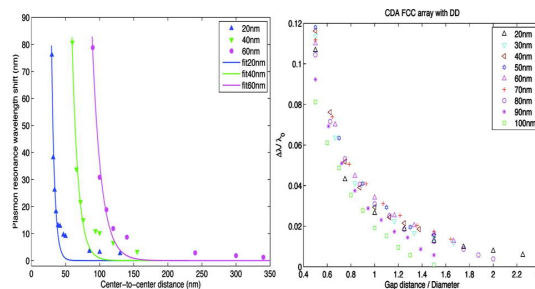


**Figure 8 A.** DDA calculations of LSPR wavelength shift versus gap distance for 2D infinite, periodic arrays with nanosphere diameters of 20, 40, and 60 nm. Solid curves are the least-squares fits to the function  $y = a \exp(-(x-1.414D)/l)$ , where  $D$  is the nanosphere diameter. The corresponding decay lengths  $l$  are 4.5, 9.0, and 13.4 nm. B. DDA calculations of scaled LSPR wavelength shift versus scaled gap distance for nanosphere diameters from 20 to 100 nm. It is clear that the data for arrays composed of 80, 90, and 100 nm nanospheres deviate from the universal exponential decay curve formed by the 20-70 nm nanospheres. Reprinted with kind permission from reference 48. Copyright 2011, American Chemical Society.

They have also reported a combination of FDTD numerical calculations and semianalytical models to understand the validity of the universal plasmon ruler for a wide range of nanocylinder dimer diameters<sup>49</sup>. Their result shows that dimers with diameters smaller than about 20 nm do not follow the universal plasmon ruler. Both reported results establish a validity range for the universal plasmon ruler, which is 20 nm diameter dimers at the lower end, and 70 nm diameter dimers at the upper end.

## 5.2. 3D Plasmon Ruler

In 2011, Liu *et al.*, extended the idea of the long range plasmon ruler to three dimensions using a more complex nanoparticle structure that is sensitive to both separation and translation, as shown in Figure 9<sup>67</sup>. Their reported three-dimensional plasmonic ruler exploits the presence of two subradiative plasmonic resonances excited by near-field coupling to a plasmonic dipole antenna. Usually, in a plasmon ruler, the dipolar plasmon resonances are broad because of radiative damping. The 3D ruler has the ability to create sharp spectral features by using interactions between quadrupolar and dipolar modes by using multiple plasmonic particles placed in close proximity to each other. Figure 9 shows the design building blocks of this 3D plasmon ruler using five gold nanorods of individually controlled length and orientation. In this condition, the dipolar resonance of a single nanorod can be strongly driven by incident electromagnetic radiation. As shown in Figure 9A, since two nanorods are placed parallel to each other, under certain circumstances, quadrupolar coupling to the incident radiation occurs. As a result, it gives rise to a much sharper resonance due to significant suppression of radiative damping. In the reported 3D plasmon ruler, strong coupling between the single nanorod and the two nanorod pairs allows for the excitation of two sharp quadrupolar resonances in the broad dipolar resonance profile. Figure 9B shows the fabrication of a series of samples using high-precision electron beam lithography and layer-by-layer stacking nanotechniques. The whole metallic structure was embedded in a dielectric medium (PC403) and resided on a glass substrate, as shown in Figure 9B.

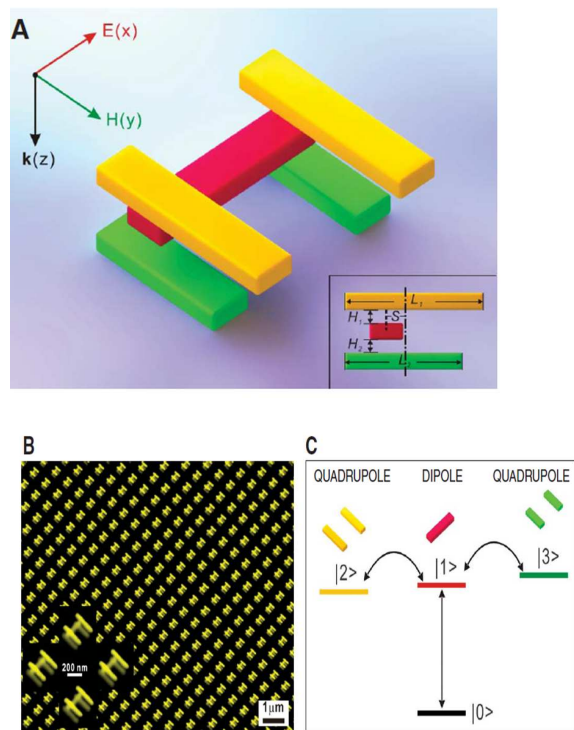


**Figure 9:** (A) Schematic diagram of the 3D plasmon ruler. (Inset) Definitions of the geometrical parameters. The red rod is displaced from the symmetry axis of the bottom green rod pair by  $S$ . The lengths of the top yellow and bottom green rods are  $L_1$  and  $L_2$ , respectively. The vertical distance between the red rod and the yellow rod pair is  $H_1$ , and that

between the red rod and the green rod pair is  $H_2$ .  $E$ , electric field;  $H$ , magnetic field;  $k$ , direction of light propagation. (B) SEM image of a typical sample fabricated by electron beam lithography. The scale bar is 200 nm. The structure is on a glass substrate. The gold rods are embedded in a photopolymer (PC403), which serves as a dielectric spacer. All the gold rods have the same thickness and width, which are 40 and 80 nm, respectively.  $S = 40$  nm,  $H_1 = H_2 = 30$  nm,  $L_1 = 340$  nm, and  $L_2 = 270$  nm. The length of the middle rod is 260 nm. The periods in both the  $x$  and  $y$  directions are 700 nm. The in-plane distance between the two rods in each rod pair is 150 nm. (C) Level scheme for two quadrupolar resonances that are coupled to a dipole in a schematic four-level system. Resonance I results from destructive interference between pathways  $|0\rangle - |1\rangle$  and  $|0\rangle - |2\rangle - |1\rangle$ . Resonance II results from destructive interference between pathways  $|0\rangle - |1\rangle$  and  $|0\rangle - |1\rangle - |3\rangle - |1\rangle$ . Reprinted with kind permission from reference 67. Copyright 2011, American Association of the Advancement of Science.

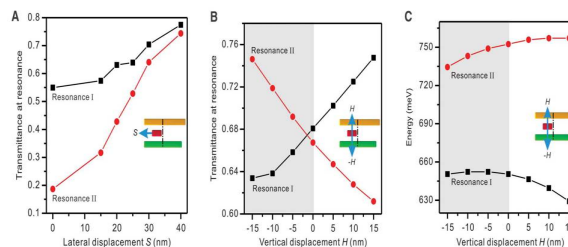


**Figure 10:** (A) Transmittance intensities of the two quadrupolar resonances in dependence on lateral displacement  $S$ , which are extracted from the experimental transmittance spectra. When  $S$  is successively decreased, both quadrupolar resonances become smaller. Resonance II diminishes much faster than resonance I. (B) Transmittance intensities of the two quadrupolar resonances in dependence on  $H$ , which is extracted from the transmittance spectra in Fig. 3B. The two resonance branches show opposite distance dependence and cross one another. (C) Spectral positions of the two quadrupolar resonances in dependence on  $H$ , which are extracted from the transmittance spectra. Resonances I and II exchange their distance-dependence behavior in  $H > 0$  (white) and  $H < 0$  (gray) areas. The sensitive behavior of the spectral features allows for extraction of the 3D structural changes. Reprinted with kind permission from reference 67. Copyright 2011, American Association of the Advancement of Science.

As shown in Figure 9, the red color middle nanorod is perpendicularly stacked between two parallel rod pairs, demonstrated as yellow and green. The lengths of the top yellow and bottom green rod pairs are  $L_1$  and  $L_2$ , respectively as described in Figure 9A. Also, the middle rod is displaced from the symmetry axis of the bottom green rod pair by  $S$ . In their design, the vertical distance between the red rod and the yellow rod pair is  $H_1$ . Similarly the distance between the red rod and the green rod pair is  $H_2$ . Figure 10 shows the intensities of the resonances and relation between the spatial structural changes and the optical response. It demonstrates how the full spectral behavior of the 3D plasmonic structure is correlated to the structural changes in space. The reported 3D plasmon ruler design allows evaluation of the magnitudes, as well as the directions, of structural changes. As shown in Figure 10A, when  $S$  decreases, the two quadrupolar resonances are both suppressed because of the reduced structural asymmetry. It is interesting to note that the higher-energy quadrupolar resonance, termed resonance II, subsides much faster than the lower-energy one, termed resonance I. Both resonance changes can be observed even at 40 nm distances. Figure 10B demonstrates the calculated intensities of the two quadrupolar resonances in dependence on  $H$ . As shown in Figure 10B, as  $H$  decreases, resonances I and II show opposite spectral behavior. Also, the transmittance intensities of the two resonance branches cross one another. Resonance I evolves from a broad profile to a narrower and

suppressed resonance, as noted in Figure 10B. On the other hand, resonance II grows in strength and becomes more and more pronounced. Figure 10C demonstrates the calculated spectral positions of the two quadrupolar resonances in dependence on H. As shown in the Figure 10C, when the middle rod is shifted downward, the position of resonance I stays nearly the same, whereas resonance II shifts to lower energies. On the other hand, when the middle rod is shifted upward, resonance II does not show a prominent position change, whereas resonance I shifts to significantly lower energies.

## 6. Long-Range NSET Ruler

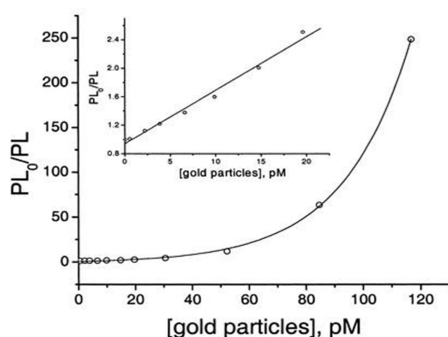


**Figure 11:** Stern–Volmer plots of polyfluorene ( $1.0 \times 10^{-6}$  M in 15 monomer repeat units) quenching by 5-nm gold nanoparticles demonstrate the hyper-efficient quenching of conjugated polymers by gold nanoparticles. Reprinted with kind permission from reference 85. Copyright 2003, National Academy of Science.

When an acceptor nanoparticle and a donor organic dye are brought into close proximity, they undergo dipole-surface type energy transfer from the dye molecular dipole to the nanometal surface which can be termed a nanomaterial surface energy transfer (NSET) <sup>86-87,96-98,102-106</sup>. Due to the huge surface plasmon enhancement, absorption cross-sections of noble gold nanoparticles are 5–7 orders of magnitude greater than with any available dye molecules. As a result, one can consider each metal nanoparticle an optical probe equivalent to several million dye molecules. Fan *et al.*, reported that nanoparticles quench the fluorescence of cationic polyfluorene with Stern–Volmer constants ( $K_{SV}$ ) approaching  $10^{11} \text{ M}^{-1}$  <sup>85</sup>. As shown in Figure 11, the emission of polyfluorene was quenched abruptly by 5-nm gold nanoparticles at sub-picomolar concentrations. The  $K_{SV}$  was measured from the photoluminescence efficiency via the relationship:

$$\frac{\phi^{\circ}}{\phi} = 1 + K_{SV}[\text{quencher}] \quad (6)$$

where  $\phi^{\circ}$  and  $\phi$  are photoluminescence quantum efficiencies in the absence and presence of the quencher, respectively. As shown in Figure 11, the plot of  $\phi^{\circ}/\phi$  vs. nanoparticle concentration demonstrates highly efficient “superquenching” produced by this fluorophore–quencher pair. The plot is linear in the concentration range of 0 to 25 pM, with  $K_{SV} = 8.3 \times 10^{10} \text{ M}^{-1}$ . It is interesting to note that the reported  $K_{SV}$  values using 5 nm gold nanoparticles are 9–10 orders of magnitude greater than small molecule dye–quencher pairs. The experimental results suggested that three factors account for this extraordinary efficiency using cationic polyfluorene, and these are: (i) amplification of the quenching via rapid internal energy or electron transfer, (ii) electrostatic interactions between the cationic polymer and the anionic nanoparticles, and (iii) the

ability of gold nanoparticles to quench via efficient energy transfer.

We have reported the particle size-dependent super-quenching properties of gold nanoparticles <sup>97</sup>. We have shown a very distinct emission intensity change from fluorophore-tagged ssRNA, when it is adsorbs onto the gold nanoparticle. Our data indicate a quenching efficiency of nearly 98% when the fluorophore was statically adsorbed onto the particle. In our experimental design, since the backbone of the single-stranded RNA was conformationally flexible, a favorable conformation for the adsorbed oligos would be an arch-like structure, in which both the 3'- and 5'-ends are attached to the particle, but the RNA chain does not contact the surface. Molecular chromophores situated in the vicinity of isolated colloidal metal particles in suspension usually experience quenching of their fluorescence, whereas photoluminescence may be enhanced in more complex structures that arise from the deposition of aggregated metal particles onto surfaces.

Dulkeith *et al.*, reported the radiative and nonradiative decay rates of dye molecules, chemically attached to differently sized gold nanoparticles <sup>87-88</sup>. As shown in Figure 12A, they have shown that when Cy5 molecules are attached to gold nanoparticles using ssDNA, they exhibit reduced fluorescence in the distance range between 2.2 and 16.2 nm. In their experiment, the changes in the radiative and the nonradiative rates with distance were monitored using time-resolved PL spectroscopy, as shown in Figure 12B. Their experimental data indicates that the nonradiative rates increased from  $1 \times 10^9$  to  $2 \times 10^9$  1/s when  $d$  was decreased from 16.2 to 2.2 nm, which shows the increasing contribution of resonant energy transfer to the nonradiative decay. They also used the Gersten–Nitzan model to interpret their experimental data. As shown in Figure 12B, the experimentally observed increase in energy transfer with decreasing distance is weaker than expected from the Gersten–Nitzan model. As a result, they concluded that the theoretical model by Gersten and Nitzan overestimates both rates but seems to predict the quantum efficiency correctly.

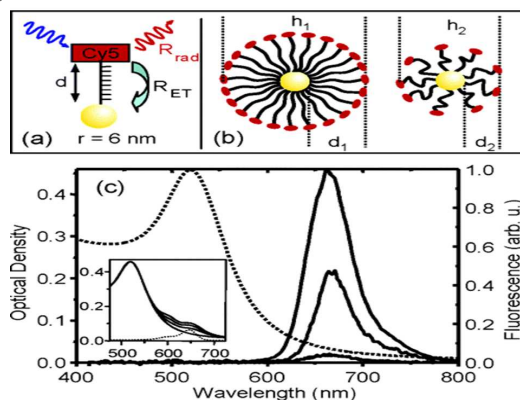


**Figure 12A:** (a) Sketch of a Cy5 dye molecule attached via a thiol-functionalized ssDNA to a gold nanoparticle of radius  $r = 6$  nm. (b) Due to limited space and repulsion, the ssDNA strands are fully stretched at a maximal surface load, providing a Cy5–AuNP distance  $d_1$ . At a reduced surface load, the ssDNA is less stretched, providing a Cy5–AuNP distance  $d_2 < d_1$ . This allows for fine-tuning of the distance  $d$ . (c) Dotted line: Optical density spectrum of a 1.94-nM AuNP solution. Solid lines in order of decreasing signal: fluorescence spectrum of a 0.24- $\mu\text{M}$  aqueous solution of pure Cy5-DNA<sub>43</sub> molecules, Cy5-DNA<sub>43</sub>–AuNP, and Cy5-DNA<sub>8</sub>–AuNP, both with the highest possible surface coverage on AuNPs. The fluorescence is reduced by 50% for Cy5-DNA<sub>43</sub> and by 95%

for Cy5-DNA<sub>8</sub>. (Inset) Solid lines: □ OD for different numbers of Cy5-DNA<sub>8</sub> molecules per AuNP (0, 64, 98, and 123 Cy5 per gold nanoparticle in order of increasing OD at 650 nm). Dotted line: □ OD of a 0.25 μM Cy5 solution. Reprinted with kind permission from reference. Copyright 2005, American Chemical Society.

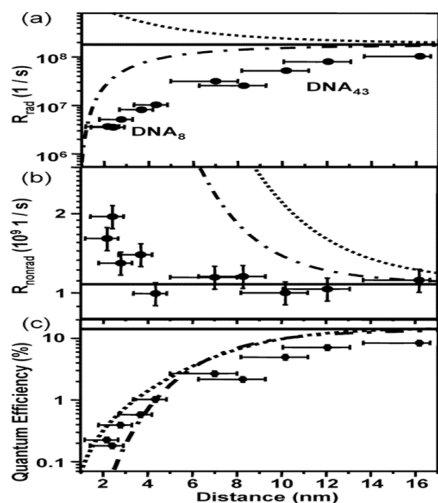


**Figure 12B:** (a) Radiative rate, (b) nonradiative rate, and (c) quantum efficiency of Cy5 molecules as a function of their distance from the gold nanoparticle surface. The solid lines are the radiative and nonradiative rates and quantum efficiencies with negligible influence of the Au NPs. Calculated radiative and nonradiative rates and the resulting quantum efficiencies are shown for molecular dipole orientations that are perpendicular (dotted lines) or tangential (dash dotted lines) to the NP surface. The experimentally-determined rates are shown as black dots. Reprinted with kind permission from reference 88. Copyright 2005, American Chemical Society.

Anger *et al.*,<sup>65</sup> reported an experimental and theoretical study of the fluorescence rate of a single molecule as a function of its distance from a laser-irradiated gold nanoparticle. As shown in Figure 13, their results indicate that the local field enhancement leads to an increased excitation rate, whereas nonradiative energy transfer to the particle leads to a decrease of the quantum yield. Due to the competing effects, by varying the distance between molecule and particle, they have demonstrated the continuous transition from fluorescence enhancement to fluorescence quenching. Due to those competing effects, their experiments showed the net luminescence can either decrease or increase depending on how the gold particle affects the chromophore's excitation rate.

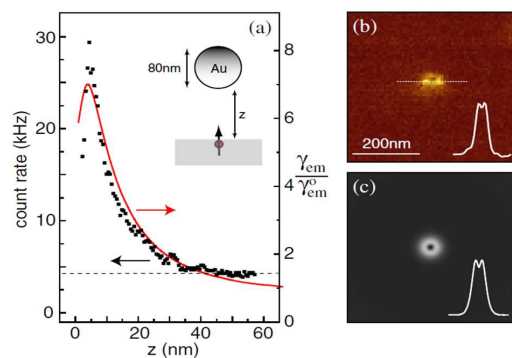


**Figure 13:** (a) Fluorescence rate as a function of particle-surface distance  $z$  for a vertically-oriented molecule (solid curve: theory; dots: experiment). The horizontal dashed line indicates the background level.

(b) Fluorescence rate image of a single molecule acquired for  $z=2$  nm. The dip in the center indicates fluorescence quenching. (c) Corresponding theoretical image. Reprinted with kind permission from reference 65. Copyright 2006, American Physical Society.

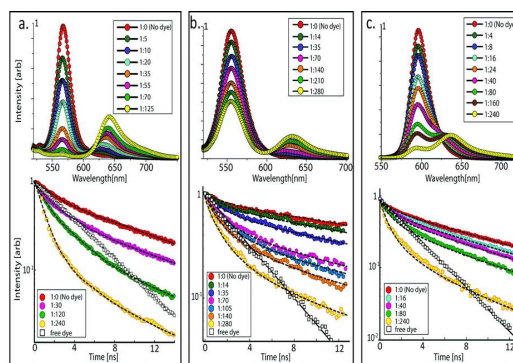


**Figure 14:** (a) Steady-state emission (top) and time-resolved spectra (bottom) for NPs with increasing ratios of Atto 590 to NP for (a) QD4.4, (b) DR93, and (c) RR. The existence of FRET between the NPs (donors) and the dye molecules (acceptors) is indicated both from steady-state emission, through quench of emission from the NPs and increase of emission from the dye, and from the temporal behavior, through the decrease in NP emission lifetime. Both phenomena increase with the addition of dye molecules per NP, obtained from spectroscopic absorption measurements, is indicated in the legends. The temporal decay of free dye is portrayed in white squares and is fitted by a single exponential. Modeled fits for emission decays are portrayed in dashed black lines, showing very good agreement with the experimental results. Reprinted with kind permission from reference 75. Copyright 2012, American Chemical Society

Since the nanoparticle has a large surface area, it allows chemical conjugation of multiple acceptors directly onto its surface, which may result in a very high NSET efficiency. Recent reports show that in such conjugated systems, the nanoparticle acts both as a donor and as a scaffold which determines the spatial distribution of the acceptors.<sup>75,86,90</sup> It also develops flexible NSET systems, where one can control the dimensionality, distance, and spatial distribution of the acceptors. Halivni *et al.*, reported the effects of the multiple donors, where nanoparticles act as donors and dye molecules chemically conjugated to the NP surface act as multiple acceptors.<sup>75</sup> Combining the model with the experimental results, they have shown that nanoparticles acting as donors can strongly affect the energy transfer characteristics in systems that consist of NPs conjugated to multiple acceptors. Their result shows that FRET lifetime is extremely sensitive to the number of attached acceptors, as shown in Figure 14.

## 6.1. Gold Nanoparticle-Organic Dye Pair NSET Ruler

Yun *et al.*, reported the first successful development of an NSET ruler using a dipole-surface type energy transfer from a molecular dipole to a nanometal surface.<sup>28</sup> As shown in Figure 15, their report demonstrates that in the case of NSET, energy transfer is possible even at a distance of 22 nm, which is more than double the traditional FRET limit. They have also demonstrated that the distance-dependent energy transfer process follows  $1/R^4$  dependence, where  $R$  is the distance between donor dye and 1.4 nm gold nanoparticle acceptor.<sup>102,128</sup> Figure 15A shows their design scheme of separating a donor fluorophore from the surface of a NP using three different lengths of dsDNA as a spacer. Gold nanoparticle-dye conjugates were prepared with the donor dye positioned on a C<sub>6</sub> spacer appended to the 5' end of a 15-base pair, a 30-base pair, and a 45-base pair synthetic dsDNA. The

distance from the center of the molecule to the metal surface was estimated by taking into account the  $C_6$  linkers and the size of the fluorescent dye. The Au-dye separation distances were  $69 \pm 5$  nm,  $120 \pm 5$  nm, and  $168 \pm 5$  nm, respectively, based on the Clegg model from the Au NP surface to the center of the donor. Since duplex DNA lengths less than 100 nm can be assumed to be a rigid rod, their construct NSET ruler distance can be calculated using simple addition of base length. Their reported results show that the short distance dependent FRET can be overcome by introducing additional transition dipoles, which provide more coupling interactions. The physical consequences of these interactions can be understood from the Fermi Golden Rule approach that relates the energy transfer ( $K_{ET}$ ) to a product of interaction elements of the donor ( $F_D$ ) and the acceptor ( $F_A$ ) as  $K_{ET} \approx F_D F_A$ . For single dipoles,  $F = 1/R^3$ , whereas for a 2D dipole array,  $F = 1/R$ , and for a 3D dipole array,  $F = \text{constant}$ , where  $R$  is the separation distance between the donor and the acceptor.

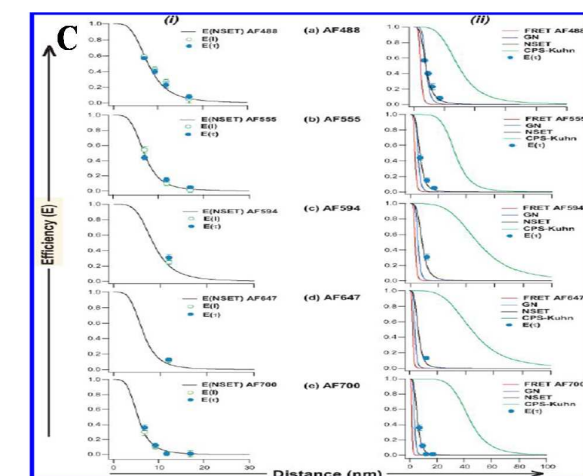
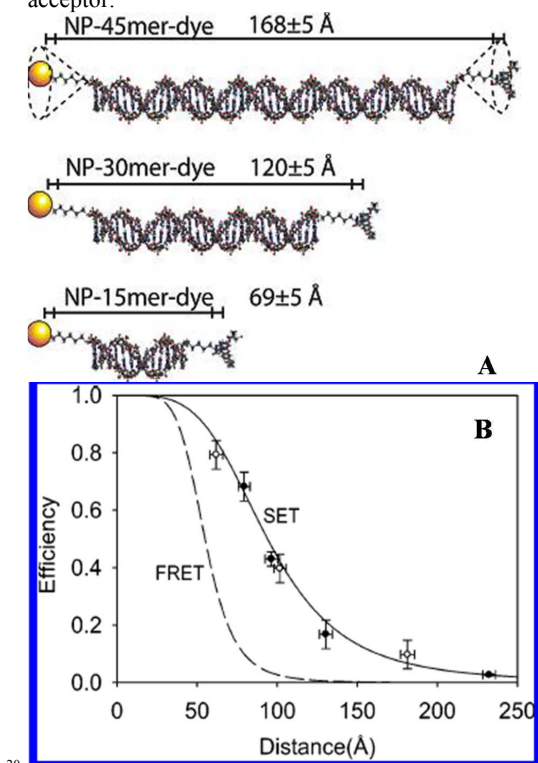


Figure 15. A) Scheme of DNA binding to a 1.5 nm Au NP. By varying the length of the DNA strand, the terminal dye fluorophore is separated from the Au NP by discrete distances (168, 120, and 69 Å). (Reprinted with kind permission from reference 102 Copyright 2006, American Chemical Society.) B) Energy transfer efficiency plotted versus separation distance between FAM and Au (nm). Filled circles (b) represent DNA lengths of 15 bp, 20 bp, 30 bp, and 60 bp. The measured efficiencies of these strands with the addition of EcoRI are represented by the open circles. The error bars reflect the standard error in repeated measurements of the fluorescence as well as the systematic error related to the flexibility of the  $C_6$  linker as illustrated in Figure 1. The dashed line is the theoretical FRET efficiency, while the solid line is the theoretical SET efficiency. (Reprinted with kind permission from reference 28. Copyright 2005, American Chemical Society.) C) (i) Efficiency curve fit of experimental PL and  $\tau$  data for (a) AF488, (b) AF555, (c) AF594, (d) AF647, and (e) AF700. (ii) Comparing the theoretical plots for three energy transfer mechanisms FRET, GN, NSET, and CPS-Kuhn models for (a) AF488, (b) AF555, (c) AF594, (d) AF647, and (e) AF700. Reprinted with kind permission from reference 128. Copyright 2010, American Chemical Society.

For the dipole-dipole FRET interaction,  $K_{ET} = F_D F_A = (1/R^3)(1/R^3) = 1/R^6$ . Now in the case of NSET, where the interaction of the dipole with the surface occurs,  $K_{ET} = F_D F_A = (1/R^3)(1/R) = 1/R^4$ . The mechanism of energy transfer intensity via coupling the oscillating electronic dipole of a dye to a metal surface with loss of energy was developed by Chance *et al.*, and by Persson *et al.*, for bulk metals<sup>112-116</sup>. The  $1/R^4$  dependence has been theoretically derived by Chance, Prock and Silbey by considering the rate of energy transfer from a dipole to a metallic surface<sup>112-114</sup>. This approach has further been extended by Persson and Lang to the metal's conduction electrons<sup>113</sup>. Figures 15B & 15C, a comparison of the experimental energy transfer efficiency values by Yun *et al.*, with the theoretical energy transfer curves for a pure dipole-dipole (FRET) and dipole-surface (SET) energy transfer process, show precisely the  $(1/R^4)$  dependence<sup>28,102,128</sup>. According to the SET model, the exact form of dipole-surface energy transfer rate can be expressed as:

$$K_{NSET} = \frac{1}{\tau_D} \left( \frac{d_0}{d} \right)^4 \quad (7)$$

where  $\tau_D$  is the lifetime of the donor in the absence of the acceptor and  $d$  is the distance between the donor and acceptor. The characteristic distance length  $d_0$  can be calculated by using the NSET equation as discussed later.

As we have stated earlier, FRET assumes the donor and acceptor as zero-dimensional resonantly-coupled oscillators operating within the limit of weak dipole coupling over distances<sup>3-14</sup>. In the case of nanoparticle-based FRET, one has to assume that the nanoparticle is a molecule and that no perturbation of the donor occurs by the surface of the nanoparticle<sup>15-22</sup>. So, in the case of nanomaterial-based FRET, the  $R_0$  values for a specific dye-metal pair can be calculated using the following equation<sup>15-22</sup>.

$$R_0^{FRET} = \left[ \frac{9000(\ln 10) \kappa^2 \Phi_{dye} J(\lambda)}{128\pi^2 N_A n^4} \right]^{1/6} \quad (8)$$

where  $\kappa$  denotes the orientation factor, and  $\Phi_{dye}$  is the Avogadro's quantum yield of the dye donor. Also,  $N_A$  is Avogadro's number, and  $n$  is the refractive index of the medium. The  $J(\lambda)$  term accounts for the overlap integral between the donor emission and the nanoparticle acceptor absorption. Several models have been developed to incorporate the presence of the metal surface in energy transfer process. According to the Gersten-Nitzan (GN) proposed theory, the nanoparticle has a

strong electric field<sup>114</sup>. When a single-point dipole, which acts as a donor, is placed close to a metal nanoparticle, there will be changes in the radiative and nonradiative rates of decay due to coupling of the donor to the metal's local electric field. In the case of the GN model, the value  $R_0^{GN}$  for a small metal nanoparticle can be expressed as:

$$R_0^{GN} = \left[ 2.25 \cdot \frac{c^3}{\omega_{dye}^3} \cdot \Phi_{dye} \cdot a^3 \cdot \frac{(\epsilon_1 + 2)^2 + \epsilon_2^2}{\epsilon_2} \right]^{1/6} \quad (9)$$

where,  $\omega_{dye}$  is the frequency of the donor dye and  $\Phi_{dye}$  is the fluorescence quantum yield of the donor. Meanwhile,  $a$  is the radius of the metal nanoparticle, and  $\epsilon_1$  and  $\epsilon_2$  are the real and imaginary components of the dielectric constant of the metal, respectively. Also,  $c$  is the speed of light. On the other hand, NSET assumes coupling between a point dipole and applies a thin film approximation to describe the two-dimensional LSPR at the surface of the metal NP<sup>28,102,128</sup>. In this case, the metal oscillators are considered to be strongly coupled, as predicted by the Drude model, rather than a collection of independent oscillating dipoles or a single dipole in analogy to the FRET model. In the case of NSET, the  $R_0^{NSET}$  value can be calculated using the following equation:

$$R_0^{NSET} = \left( 0.225 \cdot \frac{\Phi_0}{\omega_{dye}^2} \cdot \frac{1}{\omega_F \kappa_F} \cdot c^3 \right)^{1/4} \quad (10)$$

Where,  $\kappa_F$  and  $\omega_F$  are the orientation factor and frequency for the metal. Similarly,  $\omega_{dye}$  and  $\Phi_0$  represent the angular frequency of donor emission, and the fluorescence quantum yield of the donor, respectively, and  $c$  is the speed of light. Carminati et al.,<sup>115</sup> derived expressions for the distance dependence of the radiative and non-radiative rates from a point dipole interacting with proximal metallic nanoparticles, by taking into account the finite size of the nanoparticle and using Green formalism. It is known as dipole-to-metal-particle energy transfer (DMPET), where  $E_{(DMPET)}$  can be expressed as<sup>125</sup>,

$$E_{(DMPET)} = \frac{N}{N + \left( \frac{R}{R_{0(FRET)}} \right)^6 \left( 1 + \frac{1}{6} \left( \frac{2\pi m R}{\lambda} \right)^2 + \frac{1}{6} \left( \frac{2\pi m R}{\lambda} \right)^4 \right)^{-1}} \quad (11)$$

where  $R_{0(FRET)}$  is the classical Förster radius. Now, it is clear from the above equation that DMPET is a combination of FRET and NSET. So, the general form of the quantum efficiency of energy transfer can be expressed as<sup>28,102,128</sup>:

$$\Phi_{ET} \propto \frac{1}{1 + \left( \frac{r}{r_0} \right)^n} \quad (12)$$

For dipole-dipole energy transfer (FRET),  $n = 6$ , and for surface energy transfer,  $n = 4$ . Therefore, the SET process is capable of measuring longer distances than the typical Förster distances. So, the physical origin for NSET lies in the interaction of the electromagnetic field of a donor dipole with the free conduction electrons of the accepting metal. These conduction electrons interact strongly with the oscillating dipole if they travel near, and perpendicular to, the metal surface.

In order to account for the behavior of a point dipole near the metal surface, the CPS–Kuhn model assumes the metal to be a perfect mirror<sup>116-117</sup>. In their reported model, the coupling of the donor dipole to the metal leads to the potential for both enhancement and quenching, depending on the projection of the electric field from the NP surface. And it is also size dependent.  $R_0^{CPS-Kuhn}$  for the CPS–Kuhn model can be described as<sup>116-117</sup>:

$$R_0^{CPS-Kuhn} = \frac{\alpha \lambda (Aq)^{1/4}}{n} \left[ \frac{n_r}{2n} \left( 1 + \frac{\epsilon_1^2}{|\epsilon_2|^2} \right) \right]^{1/4} \quad (13)$$

where  $A$  is the absorptivity, and  $\lambda$  is the emission wavelength of the donor dipole. Similarly  $\epsilon_1$  and  $\epsilon_2$  and  $n_r$  and  $k$  are the real and imaginary components of the dielectric constant and the refractive index of the metal, respectively. Also  $n$  is the refractive index of the medium, and  $d_2$  is the thickness of the mirror.

Recently, Sing *et al.*, demonstrated that the NSET model best describes the quenching behavior for a 2 nm Au NP, whereas the CPS–Kuhn model over-predicts the distance dependence, and FRET and the GN model under-predict the distance<sup>128</sup>. As shown in Figure 15C, their experimental and theoretical data show that the FRET and CPS–Kuhn models clearly fail to fit the experimental data. On the other hand, the GN model only adequately fits AF488, but fails as the dye fluorescence wavelength is shifted toward the lower energy of the LSPR. The correlation between the NSET model predictions and the experimental results are good. They have discussed that that correlation may only be applicable to metal nanoparticles where the absorption cross-section dominates the extinction spectrum. They have also predicted that the NSET correlation is expected to fail as the Au nanoparticle size is increased, due to increasing contributions from the scattering cross-section. Recently Moroz *et al.*, reported that various approximations could be used whenever the Gersten and Nitzan theory applies for the nanoparticle based NSET<sup>114</sup>. They have shown that when particle size is  $\approx 10$  nm, one would probably be required to take into account the effect of size corrections to the bulk dielectric function. When particles are within 5 nm of one another, nonlocal effects may become important. Their results show that better modeling can be applied using modified GN theory by combining four elementary analytic functions which are responsible for residual multipole contributions. Their modeling results show that the analytic terms of the representations reveal a complex distance dependence and could be used for the qualitative and quantitative understanding of the distance behavior of nonradiative rates of fluorophores and semiconductor quantum dots involving nanometal surface energy transfer in the presence of metallic nanoparticles or nanoantennas.

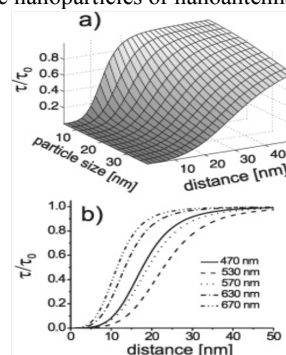


**Figure 16:** (a) Fluorescence lifetime  $\tau$  normalized to the unperturbed lifetime  $\tau_0$  of an emitter at different distances from the surface of a GNP of various diameters. (b) Normalized lifetime of an emitter placed at different separations from the surface of a GNP of diameter 15 nm and for various emission wavelengths. Reprinted with kind permission from reference 125. Copyright 2007, American Chemical Society.

Seeling *et al.*, reported the excited-state decay rate of a fluorophore attached to a gold nanoparticle at the single molecule

and single particle level<sup>125</sup>. They have discussed that the distance dependence lifetime data can be engineered by choosing the size of the nanoparticle, and it can serve as a nanoscopic ruler for measuring distances beyond what is accessible to FRET. Their data show that GNPs can modify the fluorescence lifetimes of the donor molecules. As shown in Figure 16, their results demonstrate that the rate of energy transfer between donor dye and gold nanoparticle varies with the size of the nanoparticle, as well as the distance between them. Figure 16 shows the trend of the molecular excited-state lifetime as a function of its separation distance from a GNP. Their report indicates that the change in the fluorescence lifetime close to a metallic nanoparticle can be due to the modification of the spontaneous emission or due to quenching. Figure 16a shows their reported lifetime values as a function of particle diameter, with  $d = 5 - 40$  nm. Their results show that one can tune the range and sensitivity of nanoparticle-induced lifetime modification all the way from 5 nm, which is accessible to conventional FRET, to about 40 nm by choosing GNPs of different diameters

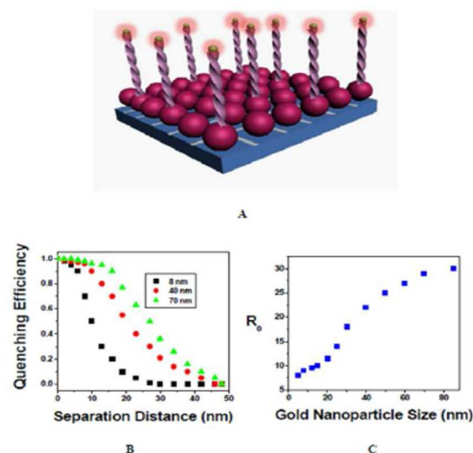


Figure 17: A) Schematic illustration of 5'Cy3 and 3'-SH modified dsRNA-based NSET ruler. B) Variation of the quenching efficiency with distance between gold nanoparticle and Cy3 dye. C) Variation of  $R_0$  with the size of gold nanoparticle. Reprinted with kind permission from reference 97. Copyright 2009, John Wiley and Sons.

We have reported how the distance-dependent NSET behavior varies with the size of the nanoparticle<sup>97</sup>. For our experiment we have used dsRNA of different lengths, so that the separation distance between a gold nanoparticle and a Cy3 dye molecule can be systematically varied between 8 nm and 50 nm, by varying the number of base pairs. As shown in Figure 17, the distance from the center of the molecule to the metal surface was estimated by taking into account size of the fluorescent dye, 0.32 nm for each base pair, and 1.8 nm for Au-S distance + base pair to dye distance. We have assumed a linear dsRNA strand configuration because ds-RNA is known to be rigid having a persistence length of 90 nm. Figure 17B shows how the quenching efficiency varies with the increase in the distance between gold nanoparticle and Cy3 dye for gold nanoparticles of different particle sizes. Our results show that the distance-dependent quenching efficiency is highly dependent on the particle size. Figure 17C shows how  $R_0$  (distance at which the energy transfer efficiency is 50%) value varies with the size of gold nanoparticles. As shown in Figure 17, our results show that one can tune the distance ranging all the way from 8 nm, which is very near to the accessible distance of conventional FRET (6 nm), to about 40 nm by choosing GNPs of different diameters. Our observations also reveal that when one chooses the experimental parameters for optimizing the NSET sensitivity, it is very important to take into account the effect of

the gold nanoparticle size, which strongly affects the quenching efficiency and distance-dependent NSET. One has to remember that due to the effect of surface charge, surface coverage, and mutual strand interaction on the bending properties of individual RNA strand, the apparent length of the oligonucleotides can be smaller than their expected molecular length.

## 6.2. Gold Nanoparticle-QD Pair NSET Ruler

Unique optical properties allow luminescent semiconductor quantum dots (QDs) to be very effective donor fluorophores for bioassays based on FRET<sup>131-140</sup>. Due to their broad absorption, coupled with size-tunable photoluminescence optimization of the spectral overlap with any potential acceptor, it is highly valuable for QDs to be donors in FRET<sup>136-146</sup>. QDs are highly photostable in comparison to common organic fluorescence dyes<sup>131-139</sup>. QDs have extremely high extinction coefficients over a broad wavelength range, and they display size-dependent emission features with narrow and symmetric emission bands with high quantum yields. In the past 15 years, various surface functionalization methods have been evaluated for attaching proteins and other biomolecules to QD surfaces<sup>131-145</sup>. Scientists have developed water-soluble and biocompatible nanocrystals, which can have wide applications in spectroscopy and microscopy of biological systems<sup>140-146</sup>. Kondon *et al.*, reported the photoluminescence quenching of a CdSe quantum dot by hexanethiolate-monolayer-protected gold clusters with core diameters of 1.1-4.9 nm<sup>131</sup>. Their reported experimental results indicate that the quenching occurs via an energy transfer mechanism. The quenching constant ( $K_Q$ ) obtained from the slope of the Stern-Volmer plot shows an enormous increase from  $2.5 \times 10^5$  to  $2.3 \times 10^8$  M<sup>-1</sup> (nearly 1000-fold) as the core size increases from 1.1 to 4.9 nm. Li *et al.*, reported the energy transfer between the QDs and the gold nanoparticles with different sizes<sup>134</sup>. Their experimental data show that the efficiency of QDs fluorescence quenching by the gold nanoparticles increases with an increase in the size of gold nanoparticles. They have shown that 80 nm sized gold nanoparticles exhibit higher quenching efficiency than the 15 nm sized gold nanoparticles. They concluded that the higher quenching efficiency for bigger nanoparticles can be attributed to an increase in spectral overlap between LSPR absorption and the emission of QDs.

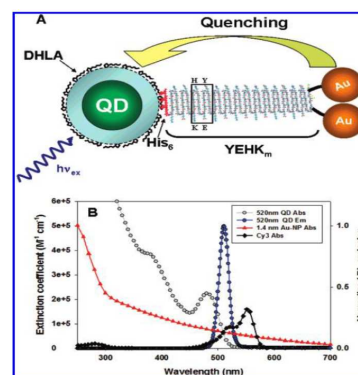
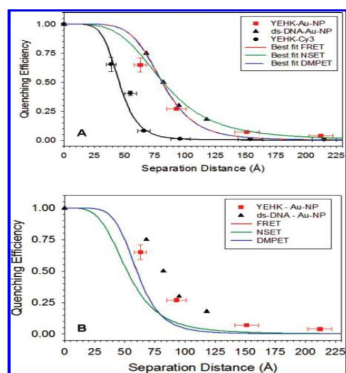


Figure 18. (A) Schematic representation of the QD-peptide-Au NP bioconjugates. The C-terminal His 6 coordinates to the QD surface while the cysteines are used as attachment sites for 1.4 nm monomaleimide-functionalized Au NPs. Repeat units of 5, 7, 14, or 21 were used; YEHK<sub>n</sub> as shown with a single core YEHK boxed. The Au NPs are separated from the cysteine thiol by a maximum of 8 Å and from each other by a maximum of 18 Å. (B) Extinction coefficient spectra of 520 nm emitting QDs, 1.4 nm Au NPs and Cy3. Normalized emission of the QDs is also

shown. Reprinted with kind permission from reference 106. Copyright 2007, American Chemical Society.

Pons *et al.*, have reported a long-range optical ruler using CdSe-ZnS quantum dots and Au nanoparticles conjugated with rigid, variable-length peptides<sup>106</sup>. In their reported experimental data, fluorescence quenching of luminescent CdSe-ZnS core-shell QDs by gold nanoparticles were performed using QD-peptide-Au NP conjugates. As shown in Figure 18, to assemble QD-Au NP pairs, they have utilized a series of engineered, variable-length de novo polypeptides. In their design, each peptide has a central block made up of several core  $\beta$ -strand repeat units, with tyrosine (Y), glutamic acid (E), histidine (H), and lysine (K) residues located at the turns of each unit. As shown in Figure 19, their experimental data show that Au NP driven QD PL quenching extends over 200 Å, which is far beyond the range allowed by FRET pairs. Using theoretical and experimental findings, they have found that cumulatively the QD PL quenching is mainly due to nonradiative energy dissipation by the Au NP without any significant modifications of the QD radiative rate. Their experimental observations indicate that the observed long-distance quenching rate is better described with a slower distance-dependence quenching rate than the classical  $1/R^6$  characteristic of Förster energy transfer. As shown in Figure 19, they have shown that the dipole-to-metal nanoparticle energy transfer model provides a better description of the distance dependence of the quenching efficiencies, even though the agreement is only qualitative since the measured values were always larger than the predicted ones. They have also tried to fit their experimental data using dipole-to-metal-particle energy transfer, (DMPET) by taking into account the finite size of the Au NP and using the Green formalism. As shown in Figure 19, the NSET model provides a better fit to the data at longer separation distances than FRET and DMPET.



**Figure 19:** PL quenching efficiency vs.  $R$  for QD-YEHK<sub>5,7,14,21</sub>-Au NP conjugates (red squares) and QD-dsDNA-Au NP from Phys. Rev. Lett. 2004, 93, (black triangles) together with best fits using FRET (red line), DMPET (blue line), and NSET (green line). The quenching efficiencies for QD-YEHK<sub>1,3,5,7,14,21</sub>-Cy3 conjugates along with a fit using Förster FRET formalism are also shown (black dots and back line). Comparison between fits and data using  $R^0$  either as a fitting parameter (A), or the experimental values deduced from the spectral overlap and QY (B). Center-to-center distances are slightly larger for the QD-peptide-Cy3 conjugates due to the presence of a larger dye linker. Horizontal error bars are the standard deviation of the distance and vertical error bars are the standard deviation of the measurement. Note that in the two panels FRET and DMPET fits overlap over the full range of distances explored. Reprinted with kind permission from reference 106. Copyright 2007, American Chemical Society.

### 6.3. Graphene Based NSET Ruler

Graphene, a single-atom-thick carbon material, exhibits remarkable electronic and thermal properties<sup>147-154</sup>. It is the basic building block of 0D fullerene, 1D carbon nanotubes, and 3D graphite<sup>155-160</sup>. Due to the nearly transparent semimetal, graphene is also a unique interface for fluorescence energy transfer. Graphene exhibits linear band dispersion around the corners of its Brillouin zone and also has a nearly constant optical absorption<sup>147-160</sup>. As a result, optically excited species can be quenched by resonant energy transfer via excitation of electron-hole pairs in graphene<sup>147-155</sup>. Chen *et al.*, have reported the efficient energy transfer from individual CdSe/ZnS nanocrystals to single- and few-layer graphenes<sup>147</sup>. Their experimental results show that strong fluorescence quenching can be observed for QD particles deposited on graphene sheets compared to the bare substrate. The reported results demonstrated that the integrated fluorescence intensities varied significantly from nanocrystal to nanocrystal, on both quartz and graphene. As shown in Figure 20, their experimental and theoretical analysis indicated the differing blinking kinetics for quartz versus graphene substrates. Their result indicates that fluorescence intensity of single nanocrystals is quenched by a factor of  $\sim 70$  on single-layer graphene. Figure 20e shows the experimental and theoretical quenching factors. The reported experimental data show the quenching factor is 70 for single layer graphene and 115 for bilayer graphene, which is in good agreement with the dipole energy transfer theory that they have used to explain their experimental data. From their results, they have discussed that fluorescence quenching by graphene should be significant at distances that cannot be reached with normal molecular donor-acceptor pairs, for which energy transfer rate decreases as  $d^{-6}$ .

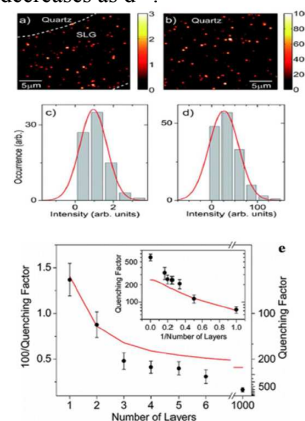


**Figure 20:** Determination of the fluorescence quenching factor. Fluorescence images and corresponding histograms of the integrated fluorescence intensities for nanocrystals on a graphene monolayer (a and c) as compared to the reference taken on a quartz substrate (b and d). The red curves in panels c and d show Gaussian fits of the histograms. The centers of the Gaussian profiles were used to calculate the average fluorescence quenching factors. e) Evolution of the fluorescence quenching factor with the number of graphene layers. The black dots represent the quenching factors for single and few-layer graphene and for graphite determined from experiment, with the corresponding experimental uncertainties. The solid lines are the quenching factors calculated from the theory. Reprinted with kind permission from reference 147. Copyright 2010, American Chemical Society.

Swathi *et al.*, reported the process of resonance energy transfer from an excited state of a donor molecule to a layer of graphene theoretically<sup>149,150</sup>. In their calculation, a simple tight binding model was used for graphene, and the rate was calculated using the Fermi Golden Rule, along with the Dirac cone approximation. As shown in Figure 21A, they have found that fluorescence

quenching can be observed up to about 30 nm for pyrene, which is much longer than FRET. Their theoretical result shows that the resonance energy transfer rate behaves like  $z^{-4}$  exactly, where  $z$  is the distance between the graphene layer and the fluorophore. Huang et al.<sup>155</sup> have shown that 50% quenching can be observed even at distance of 24 nm, when FAM dye is separated from graphene oxide (GO) through double stand DNA. Their result shows that distance dependence quenching can be described using theoretical fitting described by Swathi et al.<sup>150</sup>

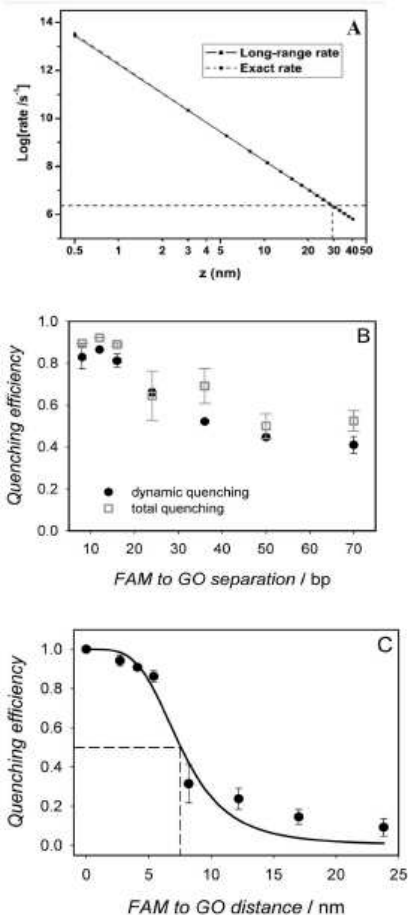


**Figure 21.** The exact rate shows the  $z^{-4}$  dependent rate. The dotted horizontal line shows the natural decay rate of pyrene. It is seen that the rate of energy transfer to graphene is comparable to this rate at a distance of 300 Å. Reprinted with kind permission from reference 150. Copyright 2009, American Institute of Physics. B) How dynamic and total quenching varies with FAM to GO separation distance. C) Theoretical fit of their experimental data. Reprinted with kind permission from reference 155. Copyright 2012, John Wiley and Sons.

## 7. Long-Range SERS Ruler

In the past 15 years, Surface-Enhanced Raman Spectroscopy (SERS) has emerged as one of the most powerful and versatile analytical tools, with detection limits down to the single molecule.<sup>161-170</sup> The possibility of observing very weak normal Raman signals, with enhancements on the order of  $10^6$ - $10^{14}$  in the presence of a metal nanomaterial surface, allow SERS to be very attractive for biological and chemical analysis.<sup>171-180</sup> In addition to the sensitivity, one of the other important features is the specificity that usually can be achieved by controlling the chemistry around the metal surface.<sup>181-190</sup> The phenomenon of very high signal enhancement in SERS is generally explained by a combination of an electromagnetic and a chemical mechanism

related to charge transfer between the substrate and the analyte molecules.<sup>191-200</sup> Since SERS can be used as a fingerprint for any species, it is also a highly valuable spectroscopic technique for chemical and biological process monitoring.<sup>180-190</sup> As a result, the development of a long-range SERS ruler will be very useful for monitoring the biological processes at a very low concentration level.

Though SERS has been used for almost thirty years, the pursuit of a full understanding of the SERS effect is still underway.<sup>161-170</sup> As we have discussed before, the Raman signal enhancement in the presence of a SERS-active substrate is attributed to two different effects.<sup>170-180</sup> The first one is the strong amplification of the electromagnetic fields near the plasmon resonances of metal substrates.<sup>168-175</sup> We and other groups have reported that the electromagnetic enhancement of Raman scattering  $E_{EM}$  can be expressed as<sup>175-180</sup>

$$E_{EM} \propto \left| \frac{E(\omega_0)}{E_0(\omega_0)} \right|^2 \times \left| \frac{E(\omega_{Raman})}{E_0(\omega_{Raman})} \right|^2 \quad (14)$$

where,  $E_{EM}$  is the average enhancement over the surface,  $E$  and  $E_0$  are the induced and incident electric field from incident laser light, and  $\omega_0$  and  $\omega_{Raman}$  are the incident laser frequency and Raman scattered frequency. The second effect to which the Raman signal enhancement is attributed in the presence of a SERS-active substrate is the chemical enhancement effect, which is mainly due to the electronic resonance process, where the charge transfer occurs between the highest unoccupied molecular orbital of molecules and the Fermi level of the metal substrate.<sup>180-190</sup> Since charge transfer enhancement is usually between 1-2 orders of magnitude, whereas the electromagnetic enhancement can be up to  $10^{16}$  orders of magnitude, in this review we will discuss mainly the electromagnetic enhancement contribution. Electromagnetic enhancement usually occurs due to the local field oscillations at the frequency of the incident radiation as a dipolar optical radiation source.<sup>161-170</sup> The distance-dependent SERS effect can be described as the dipolar field of the particle inducing a radiating dipole in the molecule, which is very similar to a London dispersion type interaction.<sup>161-170</sup> The overall distance dependence of the electromagnetic enhancement should be  $1/r^{12}$ , which indicates that SERS should be a very short range phenomenon.

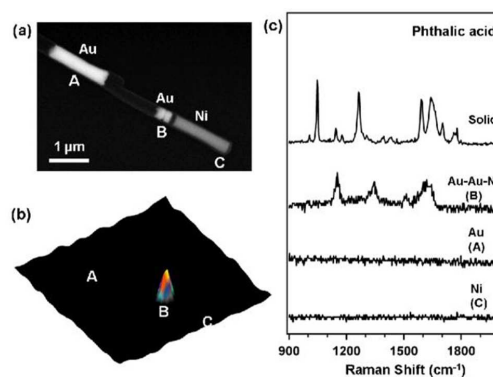


**Figure 22:** (a) Scanning electron microscopy image of Au-Ni multisegmented nanowires. Left to right: a 1.5 μm Au nanowire; a pair of  $120 \pm 18$  nm long Au nanodisks (360 nm diameter) with a  $30 \pm 10$  nm gap separated by  $120 \pm 13$  nm from a 1.5 μm Ni nanowire. The above two structures are separated by a 1.5 μm gap. (b) The corresponding confocal Raman microscopy images for nanowires in (a) functionalized with phthalic acid. (c) From top to bottom: Raman scattering of phthalic acid in the solid state; SERS spectrum of phthalic acid taken from the Ni

segment 120 nm from the Au nanodisk pair (point B in (b)); SERS spectrum of phthalic acid taken from the individual Au nanowire (point A in (b)) and Ni segment end not associated with Au nanodisk. Reprinted with kind permission from reference 162. Copyright 2009, John Wiley and Sons.

Wei *et al.*, have reported for the first time that SERS enhancement can be observed even at a 120-nm distance using Au–Ni multi-segmented nanowires<sup>162</sup>. As shown in Figure 22, their experimental data shows that disk-like Au nanostructures can be separated from the Ni segments by 120 nm and still exhibit enhanced Raman scattering by the Raman probes, even though the probes are only localized on the Ni segment. At the 120-nm distance, one can easily eliminate the possibility of hybridization of the Ni and Au plasmon resonances and the possibility of having accidental overlap with the excitation wavelength. As a result, their experimental data was an unprecedented example of long-range SERS. They have argued that the long-range enhancement leads to a more comprehensive understanding of the SPR-enhanced EM fields with the distance from the nanostructure's surface. Lal *et al.*, reported that SERS signals are easily detectable from Raman-active functional groups positioned at distances of 10 nm or more from the surfaces of the nanoparticles<sup>163</sup>. In their experimental design, a bifunctional DNA-based adsorbate molecule was used as the SERS-active molecular ruler, as shown in the Figure 23. Their SERS ruler consists of DNA with a terminal fluorescein functional group. A thiol group at the opposite end of the molecule from the fluorescein terminus allows for attachment of the molecule to the gold nanoparticle surface.

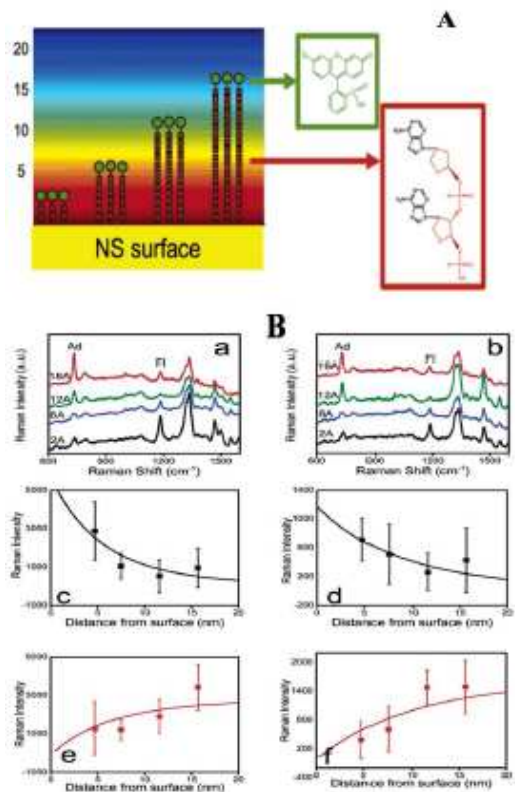


**Figure 23:** A) Schematic diagram showing the bifunctional Raman-active molecular rulers at varying distances from the nanoshell surface (y-axis). Both the terminal fluorescein and adenine strand moieties used as building blocks are shown. The SERS spectrum for each molecular component of the ruler provides an independent SERS spectrum dependent on the nanoparticle's near field. B) (a) SERS spectra for a

DNA-fluorescein adsorbate layer on  $[r_1, r_2] = [43, 58]$  nm nanoshells and (b) same as (a) but for  $[r_1, r_2] = [70, 91]$  nm nanoshells. Spectra correspond to DNA strands of 2, 6, 12, and 18 adenines, respectively. (c) SERS intensity of  $1185 \text{ cm}^{-1}$  fluorescein peak. Dots are for experimental values and solid lines for theoretically calculated values for  $[r_1, r_2] = [43, 58]$  nm nanoshells. (d) Same as (c) for  $[r_1, r_2] = [70, 91]$  nm nanoshells. (e) Same as (c) for  $736 \text{ cm}^{-1}$  adenine peak. (f) Same as (d) for  $736 \text{ cm}^{-1}$  adenine peak. Reprinted with kind permission from reference 163. Copyright 2006, American Chemical Society.

As shown in the Figure 23, their ruler provides two easily detected, independent SERS signals. The first one is from the Stokes emission of the terminal fluorescein moiety, and the second one is from the Stokes emission of the adenine groups of the DNA chain. Figure 23 demonstrates that, as the length of the adenine chain is increased, the fluorescein group extends further from the nanoparticle surface, and its SERS signal decreases with growing distance from the nanoparticle surface. On the other hand, as the adenine chain length is increased, the SERS signal from the constituent adenine groups of the chain increases as the adenine chain spans an increasing portion of the fringing field. As a result, in their report, the fluorescein and adenine moieties serve as two independent SERS reporters on the same SERS ruler, each responding to the electromagnetic field at their respective resonant frequency. As shown, the ring-breathing mode of adenine at  $736 \text{ cm}^{-1}$ , and the C–CH bending mode of the fluorescein at  $1185 \text{ cm}^{-1}$  are clearly observable. The distance-dependent intensities of the  $1185 \text{ cm}^{-1}$  mode of fluorescein and the  $736 \text{ cm}^{-1}$  mode of adenine, shows clearly that the SERS signal change can be observed even after 15 nm, which is longer than the FRET distance. They have also performed the theoretical fit, shown as solid line in Figure 23. The SERS response was calculated using Mie scattering theory. Their experimental and theoretical fit indicate that the nanoparticle surface-averaged SERS enhancement factor with distance can be expressed as:

$$G_{\text{SERS}} \propto \frac{a}{(r-r_0)^4} + \frac{b}{(r-r_0)^8} + \frac{c}{(r-r_0)^{10}} + \frac{d}{(r-r_0)^{12}} \quad (15)$$

where  $r_0$  is the effective distance from the center of the nanoshell.

In 2012, we reported development of a rigid SERS nanoruler using an oval-shaped gold nanoparticle and Rh-6G dye separated by dsDNA<sup>164</sup>. As shown in Figure 24, for the design of the SERS ruler, at first we attached 5'-Rh6G and 3'-SH modified ssDNA with the oval-shaped gold nanoparticle via thiol-gold chemistry. As shown in Figure 25, the Raman modes at  $236, 252, 273,$  and  $376 \text{ cm}^{-1}$  are N–C–C bending modes of the ethylamine group of the Rh6G ring, and the Raman modes at  $615, 778, 1181, 1349, 1366, 1511, 1570, 1603,$  and  $1650 \text{ cm}^{-1}$  are due to C–C–C ring in-plane bending, C–H out-of-plane bending, C–N stretching, and C–C stretching, as previously reported<sup>164</sup>. The Raman enhancement factor,  $G$ , is measured experimentally by direct comparison with normal Raman spectra as discussed below<sup>20-34,57</sup>.

$$G = \frac{[I_{\text{SERS}}]}{[I_{\text{Raman}}]} \times \frac{[M_{\text{Bulk}}]}{[M_{\text{Ads}}]} \quad (16)$$

where  $I_{\text{SERS}}$  is the intensity of a  $1511 \text{ cm}^{-1}$  vibrational mode in the surface-enhanced spectrum, and  $I_{\text{Raman}}$  is the intensity of the same mode in the bulk Raman spectrum from only Rh6G.  $M_{\text{Bulk}}$  is the number of molecules used in the bulk,  $M_{\text{Ads}}$  is the number of molecules adsorbed and sampled on the SERS-active substrate. All spectra are normalized for the integration time. An enhancement factor estimated from the SERS signal and normal Raman signal ratio for  $1511 \text{ cm}^{-1}$  band is approximately  $4.5 \times 10^6$ . Figure 25A shows how SERS intensity changes as we move further and further from the surface. Figure 25B shows how

change of SERS enhancement factor ( $\Delta R$ ) varies with the distance, where  $\Delta R$  is defined as the difference in SERS enhancement before and after separation. Our results show that the distance-dependent SERS is a quite long-range phenomenon.

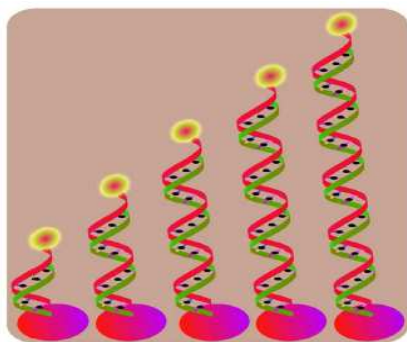


**Figure 24:** Schematic illustration of the SERS ruler that consists of 5'-Rh6G and 3'-SH modified dsDNA of different lengths attached to oval shape gold nanoparticles. Reprinted with kind permission from reference 164. Copyright 2012, American Chemical Society.

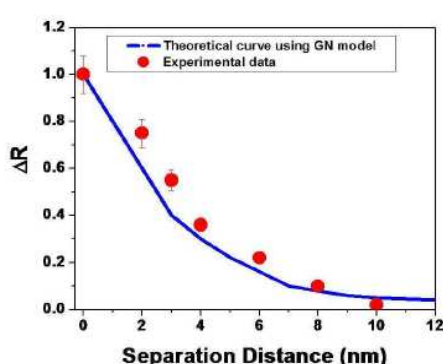
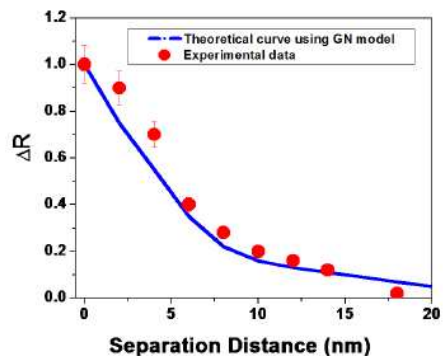
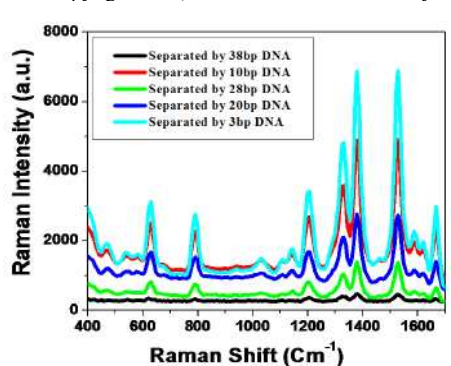


**Figure 25:** A) Plot shows how the SERS intensity from Rh6G varies when the dye is separated from the oval-shaped gold nanoparticle surface using dsDNA of different lengths. B) Plot shows how the SERS enhancement change ( $\Delta R = \text{SERS enhancement before and after separation}$ ) varies with the distance between oval-shaped gold nanoparticles of 30 nm in size and Rh6G dye when they are separated by dsDNA. It also shows theoretical fitting data for the variation of the Raman intensity with distance using the GN model. C) Plot shows how the SERS enhancement change  $\Delta R$  varies with the distance between oval-shaped gold nanoparticles of 8 nm in size and Rh6G dye when they are separated by dsDNA. It also shows theoretical fitting data for the variation of the Raman intensity with distance using the GN model. Reprinted with kind permission from reference 164. Copyright 2012, American Chemical Society.

Our results clearly indicate that the SERS signal can be easily detectable when the Raman-active dyes are positioned at distances of more than 10 nm from the surfaces of the nanoparticles. In general, the interactions between nanoparticle and Raman-active dye are quite complex due to the involvement of several parameters like excitation polarizations, wavelength, distance ranges, Raman active dye characterization, nanoparticle surface coating, and particle shape and size<sup>4-11</sup>. Light induces oscillating dipole moments in each gold particle, and their instantaneous  $1/R^3$  coupling results in a repulsive or attractive interaction, which obviously will modify the plasmon resonance of the system<sup>34-45</sup>. Due to this fact, the softer dependence of the interaction strength on particle separation distance  $r$  results in a much longer interaction range compared to  $1/R^{12}$  distance dependence, as we have observed in our experiment. To understand the experimental distance-dependent SERS phenomena, we have also performed theoretical modeling using the Gersten and Nitzan's model which is known to be useful when both the nanoparticle size ( $r$ ) and the Raman dye-to-nanoparticle distance ( $d$ ) are small compared to the excitation wavelength<sup>164,202-203</sup>. In the GN model, the Raman cross-section can be expressed as<sup>164,202-203</sup>,

$$\sigma_{\text{Raman}} = \frac{8\pi}{3} \left(\frac{\omega}{c}\right)^4 (\Delta Q)^2 \left(\frac{\partial \alpha}{\partial Q}\right)^2 \sum \left| \frac{1}{1 - \alpha G} \left( 1 + \frac{2\alpha_1^i}{(r+d)^2} \right) \right|^2 \quad (17)$$

where  $\sigma_{\text{Raman}}$  is the Raman cross-section at  $\omega$  excitation frequency, and  $\Delta \alpha$  is the induced polarizability for the molecule due to the change of nuclear coordinate ( $Q$ ). Also  $\alpha_1$  is the  $i^{\text{th}}$ -pole polarizability, which can be defined as<sup>164,202-203</sup>,

$$\alpha_i = \frac{k(\epsilon - \epsilon_M)}{i\epsilon + (k+1)} \alpha^{2i+1} \quad (18)$$

where  $\alpha_1$  depends on the metal and medium dielectric  $\epsilon$  and  $\epsilon_M$ , respectively, as well as on  $\alpha^{2i+1}$ . In the following equation,  $G$  is the image-field factor, which can be defined as<sup>164,202-203</sup>,

$$G = \sum_i \alpha_i^2 \frac{(i+1)^2}{(r+d)^{2i+1}} \quad (19)$$

The SERS enhancement ratio, which we defined as the ratio of  $\sigma_{\text{Raman}}$  in the presence and absence of nanoparticle can be expressed as<sup>164,202-203</sup>,

$$R = \left| \frac{1}{1 - \alpha G} \left( 1 + \frac{2\alpha_1^i}{(r+d)^2} \right) \right|^2 \quad (20)$$

For the calculation of  $\epsilon(\omega)$ , we have used the Drude model with damping factor  $\gamma$ , due to electron scattering, as shown below<sup>164,202-203</sup>,

$$\epsilon(\omega) = 1 - \frac{\omega_p^2}{\omega(\omega + i\gamma)} \quad (21)$$

where  $\omega$  is the laser excitation frequency and  $\omega_p$  is the plasmon frequency for nanoparticle. Figures 25B and 25C show how the SERS enhancement change ( $\Delta R = \text{SERS enhancement before and after separation}$ ) varies with distance. It is very fascinating to note from Figures 25B and 25C that the trend of distance dependent SERS enhancement change can be explained adequately using a simple GN model. To understand whether the distance-dependent SERS depends on the size of the particle, we have also performed the same experiment with 8 nm gold nanoparticle. As shown in Figures 25B & 25C, our results indicate that one can tune the SERS ruler length ranging all the way from 8 nm to about 20 nm by choosing the size of the gold nanoparticle. Though our result shows that the GN model can explain SERS enhancement change, it should be noted that experimental and theoretical correlation is better for smaller nanoparticles. The GN model considered a simple surface and used classical electrodynamics to derive the Raman cross section. If the particle size increases or if different shape particles are used, the GN model needs to be extended by accounting for nonlocal dielectric effects, nonlocal optical effects, extraneous surface charges, and higher multipolar responses, as discussed in several previous publications<sup>202-207</sup>.

## 8. Application in Biological and Chemical Process Monitoring

As the development of a long-range optical ruler has matured over the past ten years, researchers have developed ever more sophisticated control over the design and synthesis of nanoparticles with controlled functionality. As a result, numerous applications have been developed to monitor dynamical changes within nanoscale distance induced by chemical or biological processes<sup>28,29,35-40,96-110</sup>. The development of a mechanistic understanding of DNA/RNA cleavage, RNA-folding, and protein-RNA/DNA interactions would benefit from dynamics studies, where it becomes possible to detect transient intermediates and multiple reaction pathways. Although the long-range optical ruler approach is still in its infancy, proof-of-principle experiments have demonstrated that some nanomaterial-based optical rulers can already be used to investigate structural fluctuations in monitoring nuclease-catalyzed DNA or RNA cleavage reactions, RNA folding mechanisms, DNA-protein interactions, and other biological processes<sup>28,29,35-40,96-110</sup>.

### 8.1. Biological Process Monitoring Using Plasmon Ruler

Sonnichsen *et al.*, have demonstrated for the first time that a plasmon ruler can be used for studying the kinetics of single DNA hybridization events<sup>29</sup>. The plasmon rulers allowed them to continuously monitor separations of up to 70 nm for >3,000 s. Reinhard *et al.*, have reported that plasmon rulers can be used to monitor the kinetics of the cleavage of DNA by the restriction enzyme EcoRV<sup>38</sup>. DNA bending plays a crucial role in determining the specificity of DNA-protein recognition, transcription regulation, and DNA packaging. As shown in Figure 26, using plasmon rulers, they were able to follow certain steps in the catalytic cycle of EcoRV. Their reported experimental data show that using the plasmon ruler, one can directly observe DNA bending immediately preceding cleavage, which helps to understand the standard model of how the EcoRV enzyme works. As shown in Figure 27, by analysis of the interparticle potentials, they were able to see the softening of the DNA resulting from its interactions with the enzyme before cleavage. They have concluded that the unlimited lifetime, high temporal resolution,

and high signal/noise ratio allow the plasmon ruler to be a unique tool for studying macromolecular assemblies and conformational changes at the single-molecule level.

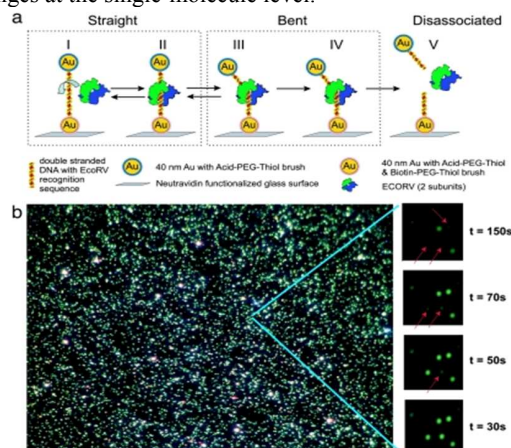


**Figure 26:** Highly parallel single EcoRV restriction enzyme digestion assay. (a) The plasmon rulers are immobilized with one particle to a glass surface through biotin–Neutravidin chemistry. The homodimeric EcoRV enzyme binds nonspecifically to DNA bound between the particles (I), translocates and binds to the target site (II), bends the DNA at the target site by  $\sim 50^\circ$  (III), cuts the DNA in a blunt-ended fashion by phosphoryl transfer (IV), and subsequently releases the products (V). (b) A  $150 \times 100\text{-}\mu\text{m}$  field of view with surface immobilized plasmon rulers. Individual dimers are visible as bright green dots. Dimer dissociation upon EcoRV-catalyzed DNA cleavage leads to a strong change in scattering intensities. The dimers are converted into monomers as shown for selected particles (red arrows, right side bar). EcoRV is added at  $t = 0$  s. Reprinted with kind permission from reference 38. Copyright 2007, National Academy of Science.

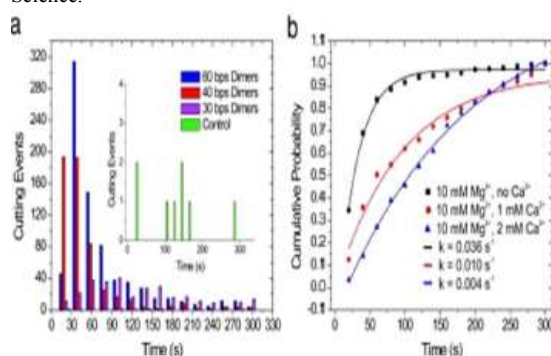


**Figure 27:** Statistical analysis of EcoRV restriction digestion of plasmon rulers. (a) The cleavage reaction is highly specific. For all DNA spacers with an EcoRV restriction site, hundreds of cutting events are observed, and in the control experiments (60-bp dimer) without a restriction site, the cutting efficiency is almost zero. Each histogram contains the combined results of two independent cutting experiments per spacer length performed with similar surface coverage. (b) Percentage of plasmon rulers that have been cleaved as a function of time for increasing  $\text{Ca}^{2+}$  concentrations. First-order kinetic fits are shown as continuous lines. EcoRV requires  $\text{Mg}^{2+}$  as a natural cofactor to catalyze DNA cleavage.  $\text{Ca}^{2+}$  can replace  $\text{Mg}^{2+}$  and facilitates formation of the enzyme–DNA complex, but the resulting complex does not catalyze the phosphodiester bond cleavage.  $\text{Ca}^{2+}$  inhibits the cleavage reaction in the presence of  $\text{Mg}^{2+}$ . A  $\text{Mg}^{2+}$  concentration of 10 mM was retained throughout. Reprinted with kind permission from reference 38. Copyright 2007, National Academy of Science.

Skewis *et al.*, have reported that plasmon rulers can be used to monitor the influence of spermidine on the cleavage kinetics of RNA by ribonuclease<sup>70</sup>. They have investigated the modulation of the activity of ribonuclease A by triamine spermidine using

plasmon ruler. Since Ribonuclease A cleaves only single-stranded RNA at the 3' end of cytosine and uracil residues, cleavage events will lead to a clear drop in scattering intensity of the plasmon ruler. As shown in Figure 28, using pairs of RNA-tethered 40 nm gold nanoparticles and time-resolved cleavage experiments, they have analyzed the influence of spermidine on the cleavage kinetics of RNase A at the single-molecule level. Their experimental results indicate that with increasing spermidine concentration, cleavage is delayed and discrete subpopulations with longer lifetimes emerge. They have explained their observation as the formation of RNA structures that are transiently stabilized against enzymatic degradation by spermidine. Their experimental data demonstrate that the plasmon rulers were able to retrieve obscured information about weak structural stabilizations such as weak secondary and tertiary structural changes. Jun *et al.*, have reported that crown nanoparticle plasmon rulers can be used for continuous observation of caspase-3 activity<sup>43</sup>. They have demonstrated an *in vivo* application of the plasmon ruler in a study of caspase-3 signaling at the single-molecule level in living cells. Their experimental data show that plasmon ruler will be able to monitor caspase-3 activation for over 2 h, unambiguously identifying early-stage activation of caspase-3 in apoptotic cells.

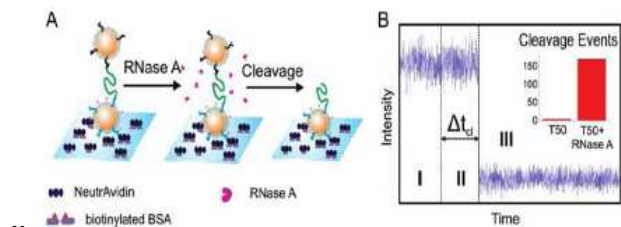


**Figure 28:** Plasmon ruler RNase A cleavage assay. (A) The RNA plasmon rulers are bound to the surface of a glass flow chamber using BSA (bovin serum albumin)-biotin-neutravidin surface chemistry. Upon addition of RNase A, the RNA tether is cleaved, and the dimer converted into a monomer. (B) Single RNA plasmon ruler cleavage trajectory (recorded at 96 Hz). (I) The plasmon ruler is first incubated in buffer containing spermidine at defined concentrations (0 -5 mM), (II) the buffer is exchanged with a 1 nM RNase A solution, causing (III) a strong drop in intensity upon RNA cleavage. Inset: Number of cleavage events for flushing with/without enzyme.  $\Delta t_{cl}$  is defined as the time between enzyme addition and cleavage. Reprinted with kind permission from reference 70. Copyright 2008, American Chemical Society.

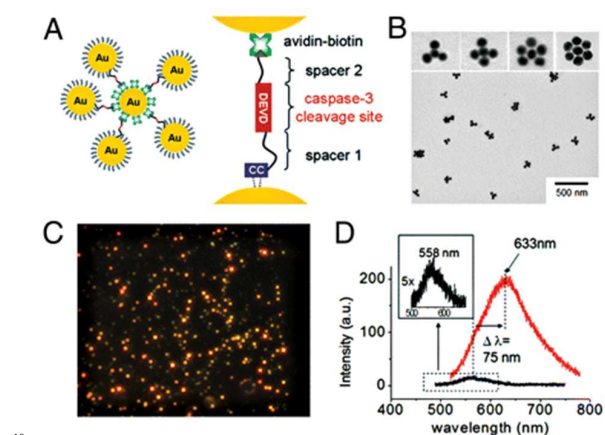


**Figure 29:** Crown nanoparticle plasmon rulers. (A) Schematic of crown nanoparticle probes, which are composed of a neutravidin-coated gold-core nanoparticle with multiple biotinylated gold satellite nanoparticles. Peptides with the caspase-3 cleavage sequence DEVD crosslink the core

and satellite nanoparticles via avidin-biotin interactions. (B) Transmission electron microscopy (TEM) of crown nanoparticles. Approximately 3 - 6 satellite nanoparticles are linked to the core nanoparticle. (C) A representative scattering image of crown nanoparticles. Intense and bright red-colored spots correspond to a single-crown nanoparticle. (D) Representative scattering spectra of a single-crown nanoparticle (red) and a single gold nanoparticle (black). A single crown nanoparticle probe exhibited a significant red shift ( $\Delta\lambda = 75$  nm) and highly increased scattering intensity ( $\sim 44$  times) compared with a single gold nanoparticle. Reprinted with kind permission from reference 43. Copyright 2009, National Academy of Science.

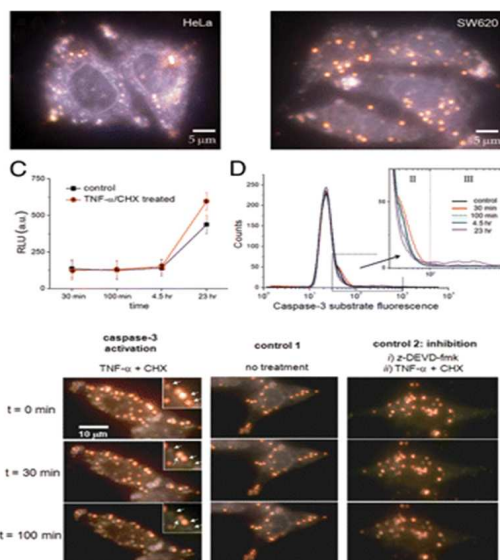


**Figure 30:** Cellular delivery of crown nanoparticles in live cells and their utilization for single-molecule imaging of caspase-3 activation in apoptotic cells. (A and B) Crown nanoparticles were first conjugated with the cell penetration peptide TAT and delivered into HeLa cells and colon cancer cells SW620. Bright red-colored spots correspond to individual crown nanoparticles. (C and D) Ensemble caspase-3 activity was measured by either by the luminescence assay (Caspase-Glo 3/7; Promega) or by the flow cytometry 30 min, 100 min, 4.5 h, and 23 h after the addition of TNF- $\alpha$ /CHX. (C) The luminescence assay shows minimal caspase-3 activation at early stages. TNF- $\alpha$ /CHX induced caspase-3 activation is evident only at 23 h. (D) Flow cytometry findings are consistent with the luminescence assay. Shoulder peaks that might be indicative of caspase-3 activity appear at early time points. (E-G) Caspase-3 activation was induced by the addition of the apoptotic inducers TNF- $\alpha$  and CHX. As time elapses, some red spots turn into either dim red or green dots. (H-J) Vehicle-treated cells show almost no signal change during the entire observation time. (K-M) Cells were pretreated with the caspase-3 inhibitor z-DEVD-fmk, and subsequently treated with TNF- $\alpha$ /CHX. There are no indications of proteolysis throughout the time course. Reprinted with kind permission from reference 43. Copyright 2009, National Academy of Science.

Their experimental data show that the plasmon ruler can be established as a robust tool for single-molecule imaging in live cells. Since FRET is limited by much shorter continuous observation windows or discontinuous snapshot imaging, the above experiment is not possible with conventional single-molecule imaging techniques. As shown in Figure 29, in their design, the assemblies are linked together by peptides containing the DEVD sequence via neutravidin-biotin and Au-thiol chemistry. They have used caspase-3 to cleave the DEVD sequence most efficiently. To deliver the neutravidin-functionalized crown nanoparticle probes inside of cells, bio-conjugated nanoparticles were conjugated with a biotinylated form of the cell penetration peptide TAT. As shown in Figure 30,

the bright red spots inside suggest successful delivery of the plasmon rulers. The experimental data show that without TAT modification, there was no indication of the nanoparticle delivery inside cells. The scattering signals from the plasmon rulers are highly intense in comparison to the background scattering from the cell. The reported data also show that the scattering signal lasts more than 8 hours under continuous illumination of visible light. They have also demonstrated no signal decrease in healthy cells, even after 8 hours of illumination, which clearly indicates that the plasmon ruler will allow the detection of single-particle trajectories with high temporal resolution during caspase-3 activation.

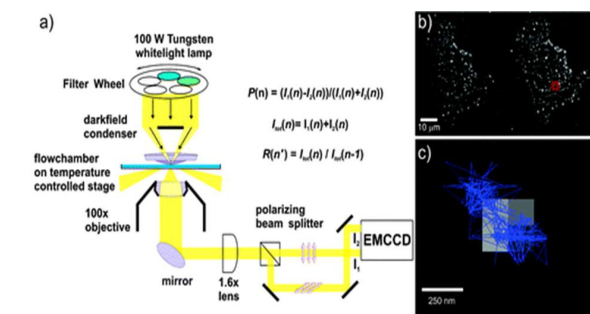


**Figure 31:** Experimental setup for polarization resolved plasmon coupling microscopy (PRPCM). (a) In a microscope with darkfield configuration the samples are illuminated with unpolarized light with alternating excitation wavelengths. The light scattered from individual nanoparticle dimers is collected with a 100X objective and then split into two orthogonal polarization channels that are re-imaged on two translated regions of an electron multiplying charge-coupled device (EMCCD). The intensities  $I_1$  and  $I_2$  on the two polarization channels in each frame  $n$  are used to calculate the reduced linear dichroism  $P$ , and the total intensities of two subsequent frames are used to calculate the intensity ratio  $R$ . (b) Image of silver plasmon rulers bound to a HeLa membrane on two orthogonal polarization channels. (c) Trajectory of an individual plasmon ruler marked in (b). The figure shows the scattering image at  $t = 0$  and the fitted position of the maximum as function of time as blue trace. Reprinted with kind permission from reference 66. Copyright 2010, American Chemical Society.

Recently Rong *et al.*, have reported that silver plasmon rulers can enable distance and orientation measurements on the nanoscale<sup>66</sup>. They have shown that the plasmon ruler can be used to monitor the translational and rotational mobility of individual rulers on lysed HeLa cells with a temporal resolution of 500 Hz. As shown in Figure 31, silver dimers on a cell membrane can be simultaneously recorded on two orthogonal polarization channels. In their experiment, individual dimers were simultaneously tracked on both channels by fitting the dimer image on two polarization channels  $I_1$  and  $I_2$ . Their experimental data show that the plasmon ruler undergoes large differences in the rotational dynamics, which was attributed to the lateral heterogeneity of the membrane. Their reported data demonstrate that the plasmon ruler has enabled a detailed structural characterization of individual membrane compartments. It can provide a quantitative metric to characterize the structural lateral heterogeneity of cell membranes on the sub-micrometer scale.

## 8.2. Biological and Chemical Process Monitoring Using NSET Ruler

Jennings *et al.*, have demonstrated for the first time that NSET can be used for an optical biomolecular kinetics study<sup>103</sup>. They have reported the structural changes and cleavage kinetics of a

synthetic 40-nucleotide hammerhead complex consisting of a ribozyme strand and a substrate strand, using NSET. Figure 32 shows the model 40-nt hammerhead complex structure that has been used for their experiment. The hammerhead is known to be a naturally-occurring RNA motif consisting of a conserved core loop flanked by three stems and is capable of catalyzing internal strand cleavage. As shown in the figure 32, at high  $Mg^{2+}$  concentration, the native ribozyme folds about the scissile bond, at  $C^*$ , which brings stems I and III into close proximity. This process initiates the cleavage of the substrate strand and finally releases the cleaved strands.

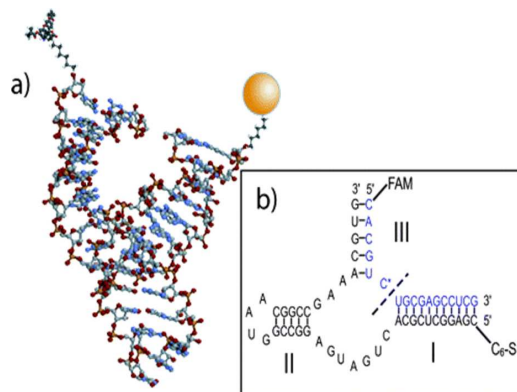


**Figure 32:** (a) Three-dimensional scheme of a hammerhead complex containing fluorophore and gold nanoparticle. (b) Secondary structure of the I/III hammerhead design used in these studies, which employs a fluorescein modifier on the substrate strand and a free thiol on the ribozyme strand. The thiol is used to bind to a 1.4-nm gold nanoparticle. Cleavage of the substrate occurs at the “scissile” bond (dashed line). Upon cleavage, the portion of the substrate with the fluorescein reporter is released outside of the quenching radius of the nanoparticle. Reprinted with kind permission from reference 103. Copyright 2006, American Chemical Society.

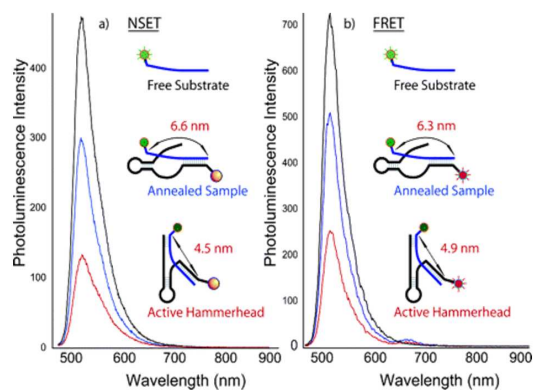


**Figure 33:** Photoluminescence quenching-correlated structural changes in the hammerhead ribozyme via energy transfer from FAM dye to nano gold (NSET, part a) and from FAM to AF647 (FRET, part b). The most intense spectrum shows the intensity of the substrate alone, and then after annealing with quencher-bound ribozyme (blue). Finally, the solution is adjusted to 20 mM  $Mg^{2+}$ , and PL is measured again (red). Reprinted with kind permission from reference 103. Copyright 2006, American Chemical Society.

As shown in Figure 33, their experimental results show that both NSET and FRET experiments exhibit fluorescence quenching of the donor FAM. Fluorescence is quenched by 39% for NSET and by 29% for FRET (relative to the control) upon formation of the hammerhead structure. They have noted a further intensity

reduction following the addition of 20 mM  $Mg^{2+}$  (68% NSET and 64% FRET) via a through-space energy transfer. Their experimental results show that for both relaxed and folded states, the fluorescence from FAM is quenched less in the FRET experiments than in the NSET experiments. Figure 34a shows a fluorescent denaturing polyacrylamide gel electrophoresis image of FAM dye under UV excitation. In their polyacrylamide gel electrophoresis data, the upper band is the intact substrate strand, and the lower band is the cleaved portion with attached FAM. Figure 34b demonstrates the kinetics traces derived from the polyacrylamide gel electrophoresis data and the continuously monitored photoluminescence for the FAM at 518 nm at different time intervals. Their data show the rate of cleavage as  $k_2 = 0.014 \pm 0.001 \text{ min}^{-1}$  for polyacrylamide gel electrophoresis and  $0.013 \pm 0.001 \text{ min}^{-1}$  for NSET. They have argued that the strong agreement on observed rates verifies for the two techniques that the changes in photoluminescence intensity are directly related to ribozyme kinetics. It also suggests that the nano gold has had a minimal effect or no effect on the cleavage rate of the ribozyme.

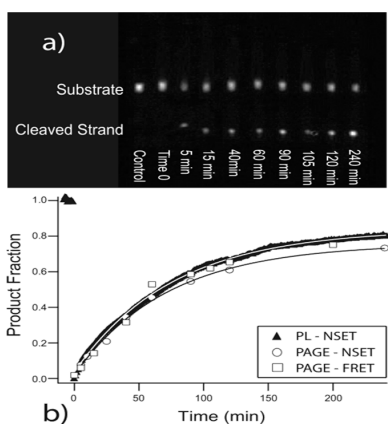


**Figure 34:** (a) Denaturing polyacrylamide gel electrophoresis of ribozyme kinetics. Each lane represents an aliquot removed from reaction at a specific time. (b) Photoluminescence intensity of FAM monitored at 518 nm. The initial intensity of FAM fluorescence decreases sharply upon addition of  $Mg^{2+}$  as the hammerhead folds into a tighter structure prior to substrate cleavage. Time-resolved PAGE aliquots using the NSET and FRET ribozyme-substrate pairs are overlaid, showing the agreement between techniques. Reprinted with kind permission from reference 103. Copyright 2006, American Chemical Society.

We have reported that gold nanoparticle-based NSET can be used to track the folding of RNA, as shown in Figure 35<sup>120</sup>. In our report, as a model system, the conformational changes of two-helix junction RNA molecules induced by the binding of  $Mg^{2+}$  ions were studied by measuring the time-dependent fluorescence signal. As shown in Figures 35 & 36, the transition from a folded to an open configuration changed the distance between the gold nanoparticle and the dye molecule attached to the ends of two helices in the RNA junction. As a result, the unfolding process was monitored by tracking the change in fluorescence intensity. As shown in Figure 36, to probe the transition states involved during the conformational change, the unfolding of the two-helix junction RNA molecules induced by  $Mg^{2+}$  ions was studied by measuring the time-dependent NSET signal. Our reported experimental results show that there are four separate states involved during the docking to undocking transition. RNAs were found to switch very slowly between the four states. As discussed in Figure 37, the changes over time in emission intensity for each state follow 1<sup>st</sup> order kinetics, for the docked configuration. The lowest emission intensity configuration is docked configuration

(D) where the two domains are in contact and at a 70° angle, as reported in the crystal structure. Since in this configuration, Cy3 dye is very near to the gold nanoparticle, the fluorescence is almost completely quenched by the gold nanoparticle. As shown in Figures 36 & 37, the highest emission intensity configuration is an extended configuration that represents the undocked state (U), where the gold nanoparticle and Cy3 dye are 43 nm apart. The other two states are transition states through which RNA folding takes place from the D → U state. To understand the structure of these two transition states, we measured distance-dependent NSET. As shown in Figure 37, our time-dependent experiments indicate that the quenching efficiency is about 98% in the D state, 85% in the 1<sup>st</sup> transition state, 45% in the 2<sup>nd</sup> transition state, and 0% in the U state. From our distance-dependent NSET and time-dependent RNA folding data, we proposed several possible transition states during folding from D → U state. In the first transition state, the two domains are in direct contact at a parallel 0° angle and start allowing for the insertion of hydrated metal ions (C). In the second transition state, the two domain surfaces are apart at a 0° angle (NC), allowing for the insertion of large amount of hydrated metal ions.

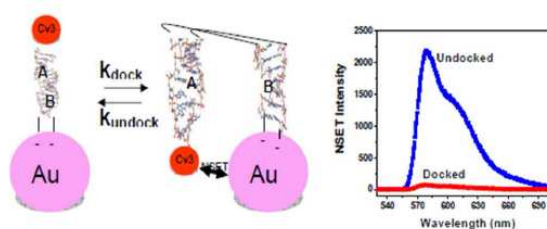


**Figure 35:** A) Schematic representation of NSET assay for RNA folding tracking. B) Time-dependent NSET intensity in presence of 15 mM  $Mg^{2+}$  at 25°C. Reprinted with kind permission from reference 120. Copyright 2008, American Chemical Society.

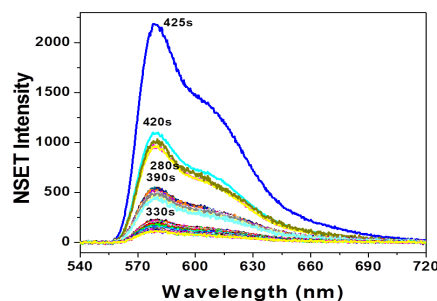


**Figure 36:** Plot showing time-dependent (in 0.1 second) NSET intensity in the presence of 15 mM  $Mg^{2+}$  at 25°C. Reprinted with kind permission from reference 120. Copyright 2008, American Chemical Society.

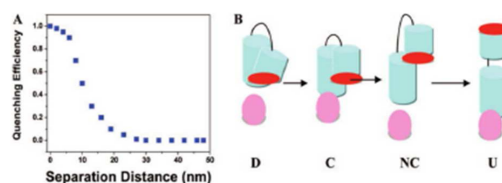


**Figure 37:** (A) Variation of the quenching efficiency with distance between gold nanoparticle and Cy3 dye. (B) Schematic representation of possible transition states involved in transition from docked to undocked state. Reprinted with kind permission from reference 120. Copyright 2008, American Chemical Society.

Chen *et al.*, have reported, for the first time, the successful construction of a NSET ruler on a live cell membrane to measure the distances between protein binding sites<sup>127</sup>. In their design, the cell membrane receptor protein tyrosine kinase 7 (PTK7) was chosen as the target molecule for the construction of the ruler. They have used monoclonal antibody anti-PTK7 and aptamer sgc8 for selective binding in the two binding sites on PTK7. For the construction of the optical ruler, gold NPs were functionalized with excess thiol-modified sgc8 aptamers on their surface. Meanwhile, the antibody anti-PTK7 was modified with the organic fluorophore Alexa Fluor 488 through the primary amines on its heavy chain. In their study, the co-localization of the two binding sites on receptor PTK7 was used to construct the energy transfer ruler. They have used confocal imaging to monitor the changes in the fluorescence energy transfer efficiency from the Alexa Fluor 488 dyes to the surface of the gold NPs. As shown in Figure 39, fluorescence quenching from the Alexa Fluor 488 donor was observed in comparison to the situation with no gold NP conjugates. Their experimental data show that when the diameters of the NPs became larger, the surface of the gold NPs were closer to the dye molecules. As a result, more fluorescence quenching was observed. By fitting distance-dependent quenching data, they obtained the distance between the two binding sites,  $R = 13.4 \pm 1.4$  nm, which is larger than the detection limit for FRET. So, their reported experimental results demonstrate that this cell membrane NSET nanoruler can measure separation distances well beyond the detection distance of FRET.

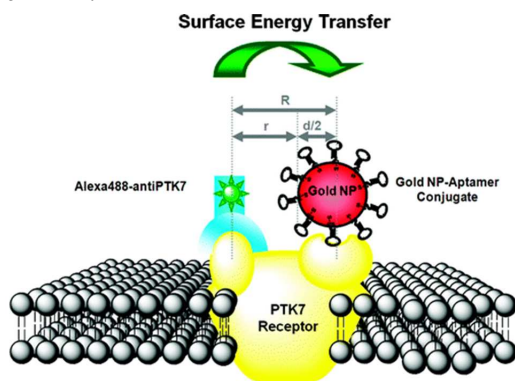


**Figure 38:** “SET Nanoruler” for measuring the distance between two binding sites in receptor PTK7 on a live cell membrane. Reprinted with kind permission from reference 127. Copyright 2010, American Chemical Society.

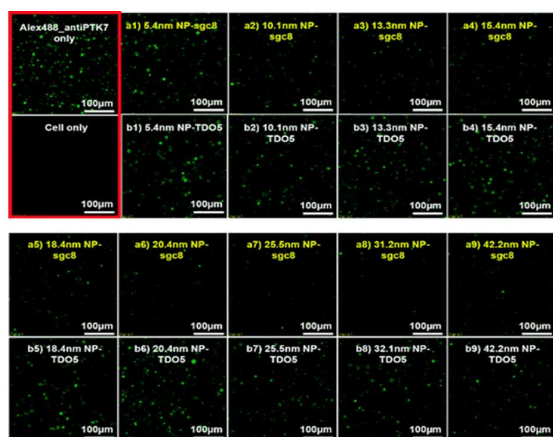


**Figure 39:** Confocal imaging assay for monitoring the fluorescence quenching on cell surfaces with different sizes of gold nanoparticles. The

two boxes framed in red show the fluorescence images of CEM cells with saturated concentration of Alexa488-labeled anti-PTK7 only and fluorescence background with cells only. Boxes (a1)-(a9) show the fluorescence of cells in the presence of different sizes of gold NP-sgc8 conjugates. Boxes (b1)-(b9) indicate the fluorescence with the control aptamers TDO5 and the same sizes of gold NPs as those shown in boxes (a1)-(a9). Vertical comparisons of the same sizes of gold NPs with aptamer sgc8 and control sequence TDO5 clearly show the difference in the fluorescence quenching efficiency. Reprinted with kind permission from reference 127. Copyright 2010, American Chemical Society.

We have reported development of a long-range nanoruler to monitor photothermal therapy response during the photothermal therapy process in human prostate cancer cells<sup>95</sup>. As shown in Figure 40, we used light-controlled photothermal release of ssDNA/RNA via dehybridization of the dsDNA/RNA complex, to monitor the photothermal therapy response. For our reported study, a well-characterized human prostate cancer cell line LNCaP which expresses a high level of prostate-specific membrane antigen (PSMA) relative to normal cells was used. Figure 39 shows our design strategy for the long-range optical ruler. We modified popcorn-shaped gold nanoparticles with an extended A9 RNA aptamer, which is specific to human prostate cancer cell PSMA. We used the extension to the A9 aptamer to serve as a hybridization site for complementary Cy3 coated RNA, which are later released during the photothermal process due to thermal de-hybridization. As a result, during the therapy process, fluorescence intensity increases, and simply by monitoring the fluorescence intensity change, one is able to monitor the *in situ* photothermal process. During photothermal therapy, the excitation laser wavelength of light is absorbed by the gold nanoparticles, and it is converted into heat by rapid electron-phonon relaxation, followed by phonon-phonon relaxation<sup>213-220</sup>. This highly localized heat generated by the gold nanoparticles kills cells selectively and also helps to optically elicit the controlled release of desired oligonucleotides which are anchored to the nanoparticles<sup>217-224</sup>.

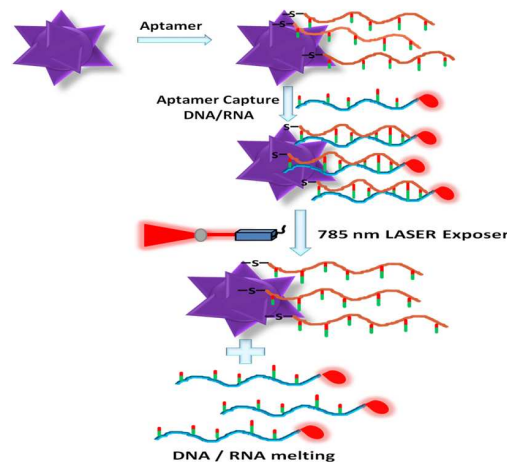


**Figure 40A:** Schematic representation showing the development of an NSET optical ruler and its working principle to monitor the photothermal therapy process. Reprinted with kind permission from reference 95. Copyright 2011, John Wiley and Sons.

As shown in Figures 40A-40B, during photothermal therapy, the lattice heat content is sufficient enough to lead to a rise in the local temperature above the melting temperature of the RNA duplex. As a result, the Cy-3 modified non-thiolated RNA strand dissociates into the surrounding medium, while its complement extended A9 RNA will remain attached to the nanoparticle. As

shown in Figure 40, our time dependent experimental results demonstrate that as the photothermal therapy progresses, the fluorescence intensity increases due to duplex RNA melting, which changes the distance between gold nanoparticle and dyes. Our reported experimental data have shown that just by monitoring fluorescence intensity change during the therapy process, one can monitor the photothermal therapy response over time. As shown in Figure 40, our experimental data indicate a nice linear plot between the percentage of cancer cell death and the fluorescence intensity change, which shows that it is highly feasible to use this long-range fluorescence assay for the measurement of *in situ* photothermal therapy response during the therapy process.

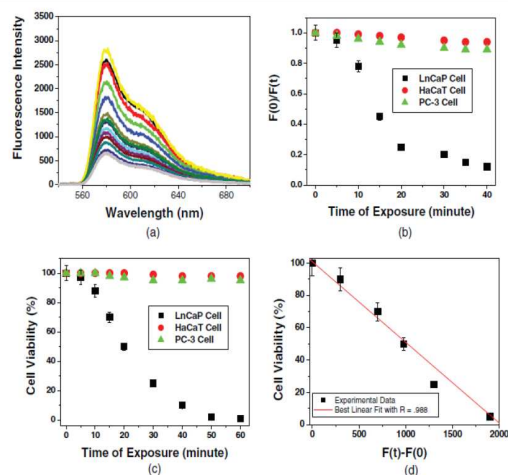


**Figure 40B:** a) Plot demonstrating time-dependent fluorescence intensity increases (2 min intervals) during nanotherapy progress of LNCaP prostate cancer cells. b) Plot demonstrating the fluorescence intensity change when extended A9 RNA-conjugated popcorn-shaped gold nanoparticles (with attached LNCaP, PC-3, and HaCaT cells) were exposed to 785 nm NIR continuous-wave radiation of different powers for 30 min. c) Plot showing cell viability measured by the MTT test after popcorn-shaped gold-nanoparticle-conjugated LNCaP, PC-3, and HaCaT cells were exposed to 100 mW, 785-nm NIR continuous-wave radiation. d) Plot showing linear relationship between % of LNCaP cell viability and NSET intensity change. Reprinted with kind permission from reference 95. Copyright 2011, John Wiley and Sons.

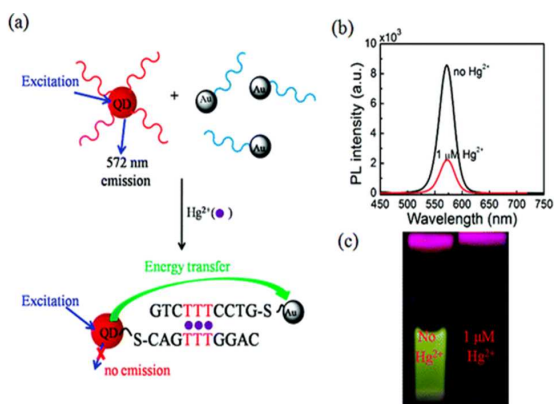


**Figure 41:** (a) Schematic illustration of the operating principle of the QD/DNA/Au NP ensemble sensor for  $\text{Hg}^{2+}$  detection. (b) Fluorescence emission spectra and (c) photograph under 365-nm laser excitation of the QD/DNA/Au NP solution (96 nM QDs, 104 nM Au NPs, and 0.1 mM ethylenediamine in 0.3 M PBS) before and after the addition of  $1 \mu\text{M}$   $\text{Hg}^{2+}$ . Reprinted with kind permission from reference 134. Copyright 2011, American Chemical Society.

Li *et al.*, have reported an NSET ruler-based sensor using a QD/DNA/Au nanoparticle ensemble for  $\text{Hg}^{2+}$  detection in water<sup>134</sup>. For the ruler development, they used QD-S-CAGTTTGGAC-3' and Au-S-GTCCTTTCTG-3' probes. In their design, two ssDNA strands are complementary, except for three deliberately designed T-T mismatches. As shown in Figure 41, in the absence of  $\text{Hg}^{2+}$ , the two probes are not capable of hybridization. As a result, fluorescence at 572 nm appears under an excitation laser. When  $\text{Hg}^{2+}$  ions are present, DNA hybridization will occur due to the formation of thymine- $\text{Hg}^{2+}$ -thymine (T- $\text{Hg}^{2+}$ -T) complexes. As a result, after  $\text{Hg}^{2+}$  addition, QDs and gold nanoparticles are brought into close proximity, which enables quenching of the fluorescence emission of the QDs. Their experimental results demonstrated that a limit of detection for their NSET ruler-based sensor is 0.4 ppb in the buffer solution

### 8.3. Biological Process Monitoring Using SERS Ruler

Bonham *et al.*, have reported an effective architecture of DNA-bridged nanoparticle assemblies for detecting concentration-dependent protein-DNA interactions<sup>168</sup>. As shown in Figure 42, in their design, duplex DNA, which was supposed to be bound by the analyte protein, was prepared by hybridization with gold nanoparticle (NP)-functionalized complementary DNA. In their design, the analyte protein was tagged with a Raman-active molecule. As shown in Figure 42, their reported assembly consists of double-stranded oligonucleotides (C) of lengths up to 39 base pairs containing the protein binding site of interest. Gold NPs are attached by thiol-modified oligo-A or oligo-B. In their experiment, the binding of DNA cytosine-C5 methyltransferase M.HhaI and yeast TBP to DNA was investigated using SERS. They have reported that their SERS-based protein-DNA assays have the ability to robustly distinguish between specific and nonspecific interactions. As shown in Figure 42B, clusters of assemblies are clearly visible at 50 $\times$  magnification. Their experimental SERS data show distinct peaks at 1342, 1584, and 1641  $\text{cm}^{-1}$  which are strong in all QSY21 spectra collected and are characteristic of the xanthene ring stretching vibrations. As shown in the Figure 42D, the SERS spectra obtained from each labeled protein with their respective cognate assemblies, shown as solid lines, display strong peaks. On the other hand, SERS peaks are not found in the noncognate samples, shown as dotted lines. So, the experimental data clearly show that a SERS-based strategy can be used to investigate protein-DNA interactions.

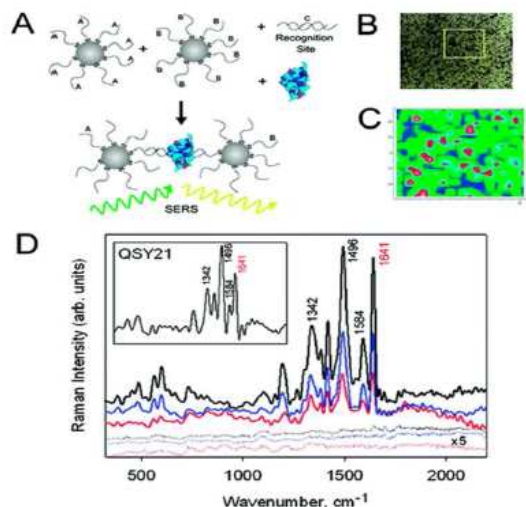


**Figure 42:** Detection of protein binding to ABC assemblies via SERS: (A) schematic of the formation of assemblies; (B) optical image of ABC assemblies deposited on glass and silver plates. Yellow rectangle indicates size of area probed by Raman mapping; (C) Raman point map of a 50- $\mu\text{m}$  X 50- $\mu\text{m}$  region, with position intensity corresponding to a peak at 1641  $\text{cm}^{-1}$  of the Raman label; (D) averaged spectra of labeled proteins: streptavidin (black), TBP (blue), and M.HhaI (red) with cognate-DNA (solid lines) and noncognate-DNA (X 5 signal, dotted lines). Background correction has been applied. Inset shows spectrum of QSY21 in silver colloid solution as a reference. The peak at 1641  $\text{cm}^{-1}$  (red) was used as the reference for comparison of signal intensity across trials. Reprinted with kind permission from reference 168. Copyright 2007, American Chemical Society.

Recently, we have reported the design of a distance-dependent SERS process for monitoring multidrug resistance photothermal lysis process<sup>213</sup>. To design the SERS ruler-based assay for monitoring the photothermal antibacterial activity process, oval-shaped gold nanoparticles were coated with double-stranded DNA, where one strand of the dsDNA strands possesses a terminal thiol moiety on its 5' end for attachment to the nanoparticle surface. As shown in Figure 43, in our design, the thiolated strand of the DNA serves as the host molecule. The complementary DNA modified with Rh-6G hybridized to the host molecule is nonthiolated. In our design, after hybridization, Rh6G-modified complementary DNA was bound only to its DNA complement host and not the nanoparticle surface. Now, in this condition, Rh-6G is placed very near to the surface and as a result, we have observed a very high SERS signal, as shown in Figure 43. Now, upon 670-nm laser illumination, during photothermal lysis, lattice heat content is sufficient enough to lead to a rise in the local temperature above the melting temperature of the DNA duplex. As shown in Figure 44, during photothermal lysis, the dsDNA was dehybridized & released the Rh-6G-modified non-thiolated DNA strand. As a result, the distance between the oval-shaped gold nanoparticles and the Rh-6G Raman dye molecules changes abruptly. Our experimental data show that the SERS intensity decreases by a huge amount. Figures 44C & 44D show the percentage of multidrug resistance bacteria (dead) vs. SERS intensity change at 1511  $\text{cm}^{-1}$ , where  $I(t)$  is the SERS intensity at 1511  $\text{cm}^{-1}$  for time  $t$ , during photothermal lysis. Meanwhile,  $I(0)$  is the initial SERS intensity at 1511  $\text{cm}^{-1}$ , before photothermal lysis begins. Our experimental data show a linear plot between percentage of MRSA bacteria killed and SERS intensity, which indicates that simple monitoring of the SERS intensity change due to duplex DNA melting can be used to monitor *in situ* photothermal antibacterial activity response.

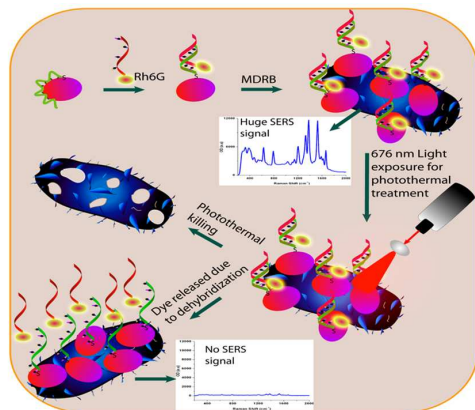


**Figure 43:** Scheme shows the development of the distance-dependent SERS assay for monitoring photothermal bacteria killing activity

response. Reprinted with kind permission from reference 213, copyright 2012, Royal Society of Chemistry.

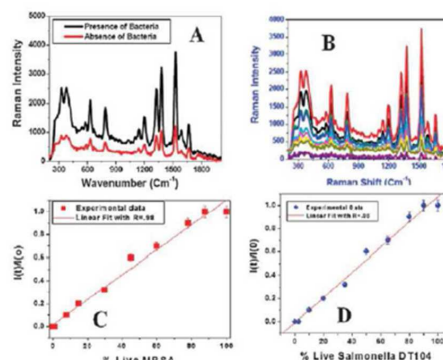


**Figure 44:** A) Plot demonstrating significant SERS intensity enhancement after the addition of  $1.3 \times 10^5$  CFU/mL MRSA, B) Plot demonstrating time-dependent SERS intensity decrease (two minutes interval) during photothermal antibacterial activity process. C) Plot showing linear relationship between % of live MRSA and SERS intensity change. D) Plot showing linear relationship between % of live Salmonella and SERS intensity change. Reprinted with kind permission from reference 213. Copyright 2012, Royal Society of Chemistry.

## 9. Summary and Outlook

In conclusion, in this review, an overview of the emerging development of long-range optical rulers is highlighted. Due to their size-dependent physical properties and nanometer-scale dimensions, nanomaterial-based rulers are attractive for various types of optical imaging, chemical assays, and nanoscale biological research. The current review highlights how the outstanding plasmonic properties of metal nanoparticles can be useful for developing long-range optical rulers. Tremendous advances have been made during the last seven years in the design of nanomaterial-based long-range optical rulers, which may provide the next generation of ultra-small devices to investigate many important fundamental questions remaining in the chemical and the biological fields. The examples of the applications involving long-range optical rulers provided herein can be readily generalized to other areas of biology and medicine because plasmonic nanomaterials exhibit great range, versatility, and systematic tunability of their optical properties. In the comparison between plasmon and NSET ruler distance measurement, plasmon ruler is highly effective in measuring distances over 100-nm range at the single-molecule level. On the other hand, NSET ruler can be used in measuring distances around 40-nm range. Since the optical properties of the plasmon ruler are based on light scattering between two nanoparticles, it is able to monitor the biological activity continuously, without any blinking, which is a huge advantage for understanding biomolecular dynamics. But, NSET optical probe works through fluorescence quenching mechanism and as a result, dye molecule needs to be incorporated for the construction of NSET ruler. Due to the presence of organic dyes, it can exhibit blinking problems for single molecule dynamics measurement. One may solve this problem by using fluorescent quantum dots. Since QDs are made from highly toxic metal ions, the toxicity of semiconductor QDs is a huge concern for in-vivo bio-applications. As an alternative, researcher may need to concentrate on the use of graphene based fluorescence quantum dots for the construction of long-range optical NSET ruler. We believe that 3D optical ruler development will improve our understanding of chemical and biological

dynamics, where the conformation of the molecules and their variation with time are important. Although the long-range optical ruler approach is still an emerging technology, proof-of-principle experiments have demonstrated that nanomaterial-based rulers can already be used to investigate structural fluctuations during chemical and biological processes. One needs to remember that since the size of nanoparticle is much bigger than an organic dye and comparable to biomolecules, interaction between DNA/RNA/protein with nanoparticle can alter the dynamical pathway of biomolecules. As our understanding of quantum plasmonics and expanded experimental capabilities advance in future, we anticipate even greater advances on nano-bio interaction in the nano-scale interface, which will help to design better long-range ruler. While this research is still in its early stages, with only a handful of successfully demonstrated cases, continued development is very important for advancing this exciting and rapidly changing research field.

The key challenge for further improvement of long-range optical ruler technology for quantitative distance measurements will be to refine colloid synthesis to obtain nanoparticles with extremely narrow size and shape distributions. The plasmon properties of individual particles depend on the particle size, and even more sensitively, on the particle shape. As a consequence, the plasmon resonance in individual plasmon rulers and the distance-dependent plasmon coupling efficiency can vary from one ruler to the next. Even after 15 years of extensive nanomaterial research, we do not have commonly accepted synthetic protocols that can be reproduced in any laboratory to synthesize a particular size and shape of nanoparticle. To take full advantage of the long-distance range ruler, synthetic strategies have to be developed to lower the surface density of tethering biopolymers and to improve the size and shape homogeneity of the nanoparticles. Another challenge in plasmonic nanomaterial-based rulers is their size, which is typically much larger than organic dyes. The nanoparticles typically have diameters in the tens of nanometers, whereas conventional organic dyes have sizes of less than 1 nm. As a result, plasmon rulers may be useful mainly for applications where unlimited probe lifetime and a larger dynamic range outweigh the drawback of larger probe size. Another important challenge that needs to be considered seriously is the possible hazards associated with these plasmonic nanomaterials.

As we have discussed, there are several advantages to using nanomaterial-based long-range optical rulers, but there still remain a number of challenges which need to be solved before it will be useful for health and environmental applications. Evaluations of human health and ecological implications of nanomaterial-based rulers have to be performed to attain full commercialization potential. In parallel for each development of long-range plasmonic ruler-based assays, the toxicity and side effects need to be addressed in a serious and systematic way as a function of the nanoparticle size, shape, and surface coating. The main question we need to understand: how toxic are the nanomaterials at the potential concentrations at which they might be used? Any toxic effects of nanomaterials will be specific to the type of base material, size, shape, and coatings. In order to know the nanoparticle hazards, we need to gain a thorough understanding of biological behavior and safety issues, such as how the nanoparticles interact with biological membranes, organelles, and biomolecules, and what their biological consequences are. We need to have knowledge of their cellular metabolism, organ toxicity, cellular excretion, and tissue accumulation, as well as an understanding of potential long-term risks before nanomaterial-based optical rulers can be used in

daily life applications. Recently, several review articles have discussed the fate, bio-distribution, and toxicity of metallic and magnetic nanoparticles and quantum dots. Most of the reported toxicity results show that gold nanoparticles are typically less toxic than other metal nanoparticles like quantum dots and magnetic nanoparticle. Several reports indicate that the modification of nanomaterial surface charge or further coating the surface greatly decreases the toxicity. It is now crucial to relate the knowledge gained from the cellular studies of nanomaterials *in vitro* with *in vivo* animal model results. Since it is well known that *in vitro* results can differ from *in vivo* results, it will be one of the most challenging research endeavors for the future which must be done before nanoparticle-based optical rulers can be used in a clinical setting.

We hope that the current review will help the readers to understand and sense the great potential of long-range optical rulers for their possible applications in chemical and biological process monitoring. It is really impressive to see the development of a new research area within the span of about seven years, along with its possible applications. Future advances will require continued innovations by chemists, physicists, and engineers, in close collaboration with experts in the medical and clinical biology fields. An increase in theoretical studies of interfaces would be of great value and will probably grow rapidly as new and challenging experimental results are reported. Advances in computer technology and the development and availability of new software and programs will be invaluable in improved modeling of the data from interfacial experiments. We believe that technology advances will improve optical ruler capability and make it possible to investigate phenomena and systems that are presently beyond our imagination, which we leave for future readers to speculate.

## 10. Abbreviations

BSA	bovine serum albumin
CFU	colony-forming unit
CHX	cycloheximidecetyltrimethylammonium bromide
1D	one-dimensional
2D	two-dimensional
3D	three-dimensional
DDA	discrete dipole approximation
DEVD	Asp-Glu-Val-Asp
DMPET	dipole-to-metal-particle energy transfer
DNA	deoxyribonucleic acid
DS	double-stranded
ELISA	enzyme-linked immunosorbent assay
EM	electromagnetic
EMCCD	electron multiplying charge-coupled device
FRET	Förster resonance energy transfer
GN	Gersten-Nitzan
GNPs	gold nanoparticles
IR	infrared
LSPR	localized surface plasmon resonance
MRSA	methicillin-resistant <i>Staphylococcus aureus</i>
MDRB	multiple drug-resistant bacteria
NIR	near infrared
NSET	nanoparticle-based surface energy transfer
PAA	polyacrylic acid
PBS	phosphate buffered saline
PL	photoluminescence
PTK7	protein tyrosine kinase 7
PSMA	prostate-specific membrane antigen
QDs	quantum dots

RNA	ribonucleic acid
Rh-6G	rhodamine-6G
SEM	scanning electron microscopy
SERS	surface-enhanced Raman scattering
5 SET	surface energy transfer
SPR	surface plasmon resonance
SS	single-stranded
TEM	transmission electron microscopy
TNF- $\alpha$	tumor necrosis factor- $\alpha$
10 UV	ultraviolet

## 11. Biographies



15 *Dr. Paresh C. Ray, Professor of Chemistry at Jackson State University, Jackson, MS, USA. He obtained his Ph.D. in Physical Chemistry from the Indian Institute of Science. Before joining JSU, he was appointed to several positions, including postdoctoral fellow at the University of Chicago, at Ohio State*  
 20 *University, and at Columbia University, NY, USA. His vision is to pursue interesting research at the interface of chemistry and biology, including exploring new strategies for developing optical rulers, creating new materials for the imaging and therapy of cancer cells and multi drug-resistant bacteria. His group's main*  
 25 *research interest is in enhancing our understanding of biomolecular interactions with nanosurfaces, as well as in developing new nano-based sensors for the detection of chemical & biological toxins from food samples. He is the author/co-author of over 140 peer-reviewed publications, with an h-index of*  
 30 *42.*



35 *Zhen Fan is currently a PhD student in the Department of Chemistry and Biochemistry at Jackson State University. His current research is mainly focused on nanoscience and nanomaterial. He is working on the research project about the interface of chemistry and biology which include exploring new material for imaging and therapy of cancer cells, multi-drug*  
 40 *resistant bacteria. He is also involved in the design of long range optical ruler.*



45 *Rebecca A. Crouch is currently a PhD student in the Department of Chemistry and Biochemistry at Jackson State University. Previously, she received her M.S. in Chemistry from Florida Atlantic University in Boca Raton, Florida, and her B.S. in Chemistry from the University of Alabama in Huntsville. Her*  
 50 *current research involves the synthesis of liposome-nanoparticle hybrids for targeted anticancer and antibacterial applications via combined photothermal and chemotherapy.*



55 *Dr. Sudarson Sekhar Sinha is currently a postdoctoral fellow at Jackson State University. He received PhD in 2013 in Chemistry from Indian Association for the Cultivation of Science, Kolkata,*  
 60 *India. In his PhD research, he studied the dynamical properties of a system coupled to a spin bath using non-equilibrium quantum statistics. His current research involves the design of the plasmonic nanoparticle base optical ruler.*



65 *Dr. Avijit Pramanik obtained his Ph.D. in 2010 from the Indian Institute of Technology (IIT) Guwahati, India, in the field of Supramolecular Inorganic Chemistry under the supervision of Prof. Gopal Das. Since then, he undertook post-doctoral research*  
 70 *at Jackson State University in Jackson, Mississippi. His current research interests are geared towards the Graphene-based nanomaterials for biosensing, bioimaging and design of long range optical ruler.*

## 75 12. Acknowledgements

Dr. Ray thanks NSF-PREM grant # DMR-0611539 and NSF-RISE grant HRD-1137763, for their generous funding.

### 13. References

1. T. Z. Förster, *Naturforsch. A* 1949, **4**, 321.
2. L. Stryer, R. P. Haugland, *Proc. Natl. Acad. Sci. USA* 1967, **58**, 719.
3. L. Stryer, *Annu. Rev. Biochem.*, 1978, **47**, 819.
4. T Ha , T Enderle, D. F. Ogletree, D. S. Chemla, P. R. Selvin, S. Weiss,  
10 *Proc. Natl. Acad. Sci. USA*, 1996, **93**, 6264.
5. S. Weiss, *Science*, 1999, **283**, 1676.
6. X. Zhuang, L. E. Bartley, H. P. Babcock, R. Russell, T. Ha, D. Herschlag and S. Chu, *Science*, 2000, **288**, 2048.
7. C. Bustamante, Z. Bryant, S. B. Smith, *Nature*, 2003, **421**, 423.
- 15 8. W. E. Moerner, D. P. Fromm, *Rev. Sci. Instrum.*, 2003, **74**, 3597.
9. B Prevo and E. J. G. Peterman, *Chem. Soc. Rev.* 2014, **43**, 1144
10. X. Michalet, S. Weiss, M. Jager, *Chem. Rev.*, 2006, **106**, 1785.
11. X. Zhuang, *Annu. Rev. Biophys. Biomol. Struct.*, 2005, **34**, 399.
12. I Rasnik, S. A. McKinney, T. Ha, *Nat. Methods*, 2006, **3**, 891.
- 20 13. M. J. Rust, M. Bates, X. Zhuang, *Nat. Methods*, 2006, **3**, 793.
14. B. Schuler, W. A. Eaton, *Curr. Opin. Struct. Biol.*, 2008, **18**, 16.
15. S. Hohng, S. Lee, J. Lee, M. H Jo, *Chem. Soc. Rev.* 2014, **43**, 1007
16. B. Schuler, E. A. Lipman, P. J. Steinbach, M. Kumke, W. A. Eaton, *Proc. Natl. Acad. Sci. USA*, 2005, **102**, 2754.
- 25 17. S W Thomas III, G D Joly, T. M. Swager, *Chem. Rev.*, 2007, **107**, 1339.
18. S. Liu, G. Bokinsky, N. G. Walter, X. Zhuang, *Proc. Natl. Acad. Sci. USA*, 2007, **104**, 12634.
19. J. Andrecka, F. Brückner, E. Lehmann, P. Cramer, J. Michaelis.  
30 *Proc. Natl. Acad. Sci. USA*, 2008, **105**, 135.
20. D. M. Jameson, J. A. Ross, *Chem. Rev.*, 2010, **110**, 2685.
21. R. Roy, S. Hohng, T. Ha, *Nat. Methods*, 2008, **5**, 507.
22. J Hohlbein, T D. Craggs and T Cordes, *Chem. Soc. Rev.* 2014 , **43**, 1156
- 35 23. T. Ha, A. G. Kozlov and T. M. Lohman, *Annu. Rev. Biophys.* 2012, 41.
24. R. H. Newman, D. Fosbrink, and J. Zhang, *Chem. Rev.*, 2011, **111**, 3614.
25. M. Y. Berezin S. Achilefu, *Chem. Rev.*, 5 2010, **110** , 2641.
- 40 26. Y. N. Teo, E. T. Kool, *Chem. Rev.*, 2012, **112**, 4221.
27. M. Vendrell, D. Zhai, C. J. Er, Y. T. Chang, *Chem. Rev.*, 2012, **112**, 4391.
28. C. S. Yun , A. Javier, T. Jennings, M. Fisher, S. Hira, S. Peterson, B. Hopkins, N. O. Reich and G. F. Strouse, *J. Am. Chem. Soc.*, 2005, **127**, 3115.
- 45 29. C. Sonnichsen, B. M. Reinhard, J. Liphardt, A. P. Alivisatos, *Nat. Biotechnol.* 2005, **23**, 741.
30. M. Faraday, *Philos. Trans. R. Soc. London*, 1857, **147**, 145.
31. K. L. Kelly, E. Coronado, L. L. Zhao, G. C. Schatz, *J. Phys. Chem. B*  
50 2003, **107**, 668.
32. P. K. Jain, X. Huang, I. H. El-Sayed, M. A. El-Sayed, *Acc. Chem. Res.* 2008, **41**, 1578.
33. N. J. Halas, *Nano Lett.*, 2010, **10**, 3816.
34. P. L. Stiles, J. A. Dieringer, N. C. Shah, R. P. Van Duyne, *Annu. Rev.*  
55 *Anal. Chem.* 2008, **1**, 601.
35. N. J. Halas, S. Lal, W. S. Chang, S. Lin, and P. Nordlander P, *Chem. Rev.*, 2011, **111**, 3913.
36. K. H. Su, Q. H. Wei, X. Zhang, J. J. Mock, D. R. Smith, S. Schultz, *Nano Letters* 2003 **3**, 1087.
- 60 37. D. C. Marinica, A. K. Kazansky, P. Nordlander, J. Aizpurua, and A. G. Borisov, *Nano Letters* 2012 **12**, 1333.
38. B. M. Reinhard, S. Sheikholeslami, A. Mastroianni, A. P. Alivisatos, J. Liphardt, *Proc. Natl. Acad. Sci. U.S.A.* 2007, **104**, 2667.
39. P. K. Jain, M. A. El-Sayed, *Nano Lett.* 2008, **8**, 4347.
- 65 40. J. N. Anker, W. P. Hall, O. Lyandres, N. C. Shah, J. Zhao, R. P. Duyne, *Nat. Mater.* 2008, **7**, 442.
41. P. K. Jain, M. A. El-Sayed, *J. Phys. Chem. C* 2007, **111**, 17451.
42. C. Tabor, R. Murali, M. Mahmoud, M. A. El-Sayed, *J. Phys. Chem. A* 2009, **113**, 1946.
- 70 43. Y. W. Jun, S. Sheikholeslami, D. R. Hostetter, C. Tajon, C. S. Craik, A. P. Alivisatos, *Proc. Natl. Acad. Sci. U.S.A.* 2009, **106**, 17735.
44. E. Prodan, C. Radloff, N. J. Halas, P. Nordlander, *Science* 2003, **302**, 419.
45. P. Nordlander, C. Oubre, E. Prodan, K. Li, M. Stockman, *Nano Lett.*  
75 2004, **4**, 899.
46. P. K. Jain, M. A. El-Sayed, *Nano Lett.* 2007, **7**, 2080.
47. L. V. Brown, H. Sobhani, J. B. Lassiter, P. Nordlander, P.; N. J. Halas, *ACS Nano* 2010, **4**, 819.
48. X. Ben, H. S. Park, *J. Phys. Chem. C* 2011, **115**, 15915–15926
- 80 49. X. Ben, H. S. Park *J. Phys. Chem. C* 2012, **116**, 18944–18951
50. A. M. Kern, D. Zhang, M. Brecht, A. I. Chizhik, A. V. Failla, F. Wackenhut and A. J. Meixner, *Chem. Soc. Rev.* 2014, **43**, 1263
51. B. M. Reinhard, M. Siu, H. Agarwal, A. P. Alivisatos, J. Liphardt, *Nano Lett.*, 2005, **5**, 2246.
- 85 52. F. Wen, J. Ye, N. Liu, P. V. Dorpe, P. Nordlander, and N. J. Halas, *Nano Letters* 2012 **12**, 5020.
53. S. A. Lee, L. Liu, K. S. Kim, and S. Park, *J. Phys. Chem. C*, 2012, **116**, 18388.
54. S. Sheikholeslami, Y. W. Jun, P. K. Jain, A. P. Alivisatos, *Nano Lett.*  
90 2010, **10**, 2655.
55. H. Chen, L. Shao, Q. Li and J. Wang, *Chem. Soc. Rev.* 2013, **42**, 2679–2724
56. S. Zhang, K. Bao, N. J. Halas, H. Xu and P. Nordlander, *Nano Lett.*, 2011, **11**, 1657.
- 95 57. A. E. Miroshnichenko, S. Flach, Y. S. Kivshar, *Rev. Mod. Phys.* 2010, **82**, 2257.
58. N. Liu, H. Liu, S. N. Zhu, H. Giessen, *Nat. Photonics* 2009, **3**, 157.
59. M. Hentschel, D. Dregely, R. Vogelgesang, H. Giessen, N. Liu, *ACS Nano* 2011, **5**, 2042.
- 100 60. J. A. Fan, C. Wu, K. Bao, J. Bao, R. Bardhan, N. J. Halas, V. N. Manoharan, P. Nordlander, G. Shvets, F. Capasso, *Science* 2010, **328**, 1135
61. M. Hentschel, M. Saliba, R. Vogelgesang, H. Giessen, A. P. Alivisatos, N. Liu, *Nano Lett.* 2010, **10**, 2721.
62. B. Luk'yanchuk, N. I. Zheludev, S. A. Maier, N. J. Halas, P.  
105 Nordlander, H. Giessen, C. T. Chong, *Nat. Mater.* 2010, **9**, 707.
63. Y. Wang, J. Xu, Y. Wang and H. Chen, *Chem. Soc. Rev.* 2013, **42**, 2930–2962
64. J. B. Lassiter, H. Sobhani, M. W. Knight, W. S. Mielczarek, P. Nordlander, N. J. Halas, *Nano Lett.* 2012, **12**, 1058.
- 110 65. P. Anger, P. Bharadwaj, L. Novotny, *Phys. Rev. Lett.* 2006, **96**.
66. G. Rong, H. Wang and B. M. Reinhard, *Nano Lett.*, 2010, **10**, 230.
67. N. Liu, A. P. Alivisatos, M. Hentschel, T. Weiss, H. Giessen, *Science*, 2011, **332**, 1407.
68. T. J. Davis, M. Hentschel, N. Liu and H. Giessen, *ACS Nano*, 2012, **6**,  
115 1291.
69. M. Hentschel, M. Schäferling, T. Weiss, N. Liu and H. Giessen , *Nano Letters* 2012, **12**, 2542.
70. L. R. Skewis and B. M. Reinhard, *Nano Lett.*, 2008, **8**, 214–220.
71. R. T. Hill, J. J. Mock, A. Hucknall, S. D. Wolter, N. M. Jokerst D. R. Smith and A. Chilkoti, *ACS Nano*, 2012, **6**, 9237.
- 120 72. M. Grzelczak and L. M. Liz-Marzán, *Chem. Soc. Rev.* 2014 , **43**, 2089
73. J. I. L. Chen, Y. Chen, D. S. Ginger, *J. Am. Chem. Soc.* 2010, **132**, 9600.
- 125 74. D. C. Marinica, A. K. Kazansky, P. Nordlander, J. Aizpurua, A. G. Borisov, *Nano Lett.* 2012, **12**, 1333.
75. S. Halivni, A. Sitt, I. Hadar, U. Banin, *ACS Nano* 2012, **6**, 2758–2765.
76. F. López-Tejiera, R. Paniagua-Domínguez, and J. A. Sánchez-Gil ,  
130 *ACS Nano* 2012 **6**, 8989.
77. V. A. Turek, M. P. Cecchini, J. Paget, A. R. Kucernak, A. A. Kornyshev, and J. B. Edel, *ACS Nano*, 2012, **6**, 7789.
78. J. H. Yoon, J. Lim, and S. Yoon, *ACS Nano*, 2012, **6**, 7199.
79. S. Kasper, F. B. Jeremy, J. Baumberg, O. A. Scherman, and S.  
135 Mahajan, *Nano Letters* 2012, **12**, 5924.
80. P. D. Nallathambay, T. Huang and X-H Nancy, *Nanoscale*, 2010, **2**, 1715–1722.
81. T. W. Johnson, J. Z. Lapin, R. Beams, N. C. Lindquist, S. G. Rodrigo, L. Novotny and H. S. Oh, *ACS Nano* 2012, **6**, 9168.
- 140 82. A. Yurtsever and A. H. Zewail *Nano Lett.*, 2012, **12**, 3334.
83. H. Duan, A. I. Fernández-Domínguez, M. Bosman, S. A. Maier and K. W. Yang, *Nano Lett.*, 2012, **12**, 1683.
84. J. M. Romo-Herrera, R. A. Alvarez-Puebla and L. M. Liz-Marzán, *Nanoscale*, 2011, **3**, 1304–1315 .

85. C. Fan, S. Wang, J. W. Hong, G. C. Bazan, K. W. Plaxco, A. J. Heeger *Proc Natl Acad Sci USA*, 2003, **100**, 6297.
86. K. Boldt, S. Jander, K. Hoppe, H. Weller, *ACS Nano* 2011, **5**, 8115–8123
87. E. Dulkeith, A. C. Morteani, T. Niedereichholz, T. A. Klar, J. Feldmann, S. A. Levi, F. C. van Veggel, D. N. Reinhoudt, M. Moller & D. I. Gittins, *Phys. Rev. Lett.*, 2002, **89**, 203002.
88. E. Dulkeith, M. Ringle, T. A. Klar, J. Feldmann, A. Munoz Javier, W. J. Parak, *Nano Lett.* 2005, **5**, 585.
89. J. Gersten, A. J. Nitzan, *Chem. Phys.* 1981, **75**, 1139.
90. M. Swierczewska, S. Lee and X. Chen, *Phys. Chem. Chem. Phys.* 2011, **13**, 9929-9942.
91. K. Aslan, C. D. Geddes, *Curr. Opin. Biotech.* 2005, **16**, 55-62.
92. H. X. Li, L. J. Rothberg, *Proc. Natl. Acad. Sci. USA*, 2004, **101**, 14036.
93. P. P. Hu, L. Q. Chen, C. Liu, S. J. Zhen, S. J. Xiao, L. Peng, Y. F. Li and C. Z. Huang, *Chem. Comm.* 2010, **46**, 8285-8287
94. K. Saha, S. A. Agasti, C. Kim, X. Li, and V. Rotello, *Chem. Rev.*, 2012, **112**, 2739–2779
95. A. K. Singh, W. Lu, D. Senapati, S. A. Khan, Z. Fan, T. Senapati, T. Demeritte, L. Beqa, and P. C. Ray, *Small*, 2011, **7**, 2517.
96. P. C. Ray, G. K. Darbha, A. Ray, J. Walker, W. Hardy and A. Perryman, *Plasmonics*, 2007, **2**, 173.
97. J. Griffin, A. K. Singh, D. Senapati, P. Rhodes, K. Mitchell, B. Robinson, E. Yu, and P. C. Ray, *Chem. Eur. J.*, 2009, **15**, 342.
98. D. Liu, S. Wang, M. Swierczewska, X. Huang, A. A. Bhirde, J. Sun, Z. Wang, M. Yang, X. Jiang and X. Chen, *ACS Nano*, 2012, **6**, 10999.
99. S. Saini, G. Srinivas, B. Bagchi, *J. Phys. Chem. B.* 2009, **113**, 1817.
100. S. R. Swathi, K. L. Sebastian, *J. Chem. Phys.* 2007, **126**, 234701.
101. F. Gao, E. Yao, W. Wang, H. Chen and Y. Ma, *Phys. Chem. Chem. Phys.* 2012, **14**, 15321-15327
102. T. L. Jennings, M. P. Singh, G. F. Strouse, *J. Am. Chem. Soc.* 2006, **128**, 5462.
103. T. L. Jennings, J. C. Schlatterer, M. P. Singh, S. N. L. Greenbaum and G. F. Strouse, *Nano Lett.*, 2006, **6**, 1318.
104. M. P. Singh, T. L. Jennings and G. F. Strouse, *J. Phys. Chem. B*, 2009, **113**, 552.
105. J. Travis, S. Geoffrey S, *Advances in Experimental Medicine and Biology*, 2007, **620**, 34.
106. T. Pons., I. L. Medintz, K. E. Sapsford, S. Higashiya, A. F. Grimes, D. S. English, H. Mattoussi, *Nano Lett.*, 2007, **7**, 3157.
107. Z. Gueroui, A. Libchaber, *Phys. Rev. Lett.* 2004, **93**.
108. T. Sen, S. SadhuA. and Patra, *Appl. Phys. Lett.* 2007, **91**, 043104.
109. T. Sen and A. Patra, *J. Phys. Chem. C*, 2012, **116**, 17307.
110. T. Sen, A. Patra, *J. Phys. Chem. C*, 2009, **113**, 13125.
111. P. Yu, X. Wen, Y.-R. Toh, Y.-C. Lee and J. Tang, *Rsc. Adv.* 2013, **3**, 19609-19616
112. R. R. Chance, A. Prock, R. Silbey, R. In Advances in Chemical Physics, Vol. 37; Prigogine, I. Rice, S. A., Eds.; John Wiley & Sons, Inc.: New York, 1978; 1.
113. B. N. J. Persson, N. D. Lang, *Phys. Rev. B*, 1982, **26**, 5409.
114. A. Moroz, *J. Phys. Chem. C*, 2011, **115**, 19546–19556.
115. R. Carminati, J. J. Greffet, C. Henkel, J. M. Vigoureux, *Opt. Commun.* 2006, **261**, 368.
116. H. Kuhn, *J. Chem. Phys.* 1970, **53**, 101.
117. O. Mnacker, and H. Kuhn, *Chem. Phys. Lett.* 1974, **27**, 317.
118. P. C. Ray, A. Fortner, G. K. Darbha, *J. Phys. Chem. B*, 2006, **110**, 20745.
119. G. K. Darbha, A. Ray, P. C. Ray, *ACS Nano*, 2007, **3**, 208.
120. J. Griffin, P. C. Ray, *J. Phys. Chem. B.; (Letter)*; 2008; **112**, 11198.
121. L. R. Skewis., B. M. Reinhard, *Nano Lett.*, 2008, **8**, 214.
122. J. S. Lee, S. M. Han, C. A. Mirkin, *Angew. Chem. Int. Ed.* **46**, 2007, 4093.
123. R. M. Clegg, A. I. H. Murchie, A. Zechel, D. M. J. Lilley, *Proc. Natl. Acad. Sci. U.S.A.* 1993, **90**, 2994.
124. R. S. Mathew-Fenn, R. Das, P. A. B. Harbury, *Science*, 2008, **322**, 446.
125. Seelig, J.; Leslie, K.; Renn, A.; Kühn, S.; Jacobsen, V.; van de Corput, M.; Wyman, C.; Sandoghdar, V. *Nano Lett.* 2007, **7**, 685.
126. S. Mayilo, M. A. Kloster, M. Wunderlich, A. Lutich, A. Klar, M. T. A. Nichtl, K. Kurzinger, F. Stefani, D.; Feldmann, *Nano Lett.* 2009, **9**, 4558.
127. Y. Chen, M. B. O'Donoghue, Y. F. Huang, H. Kang, J. A. Phillips, X. Chen, M. C. Estevez, C. J. Yang, W. Tan, *J. Am. Chem. Soc.* 2010, **132**, 16559.
128. M. P. Singh, G. F. Strouse, *J. Am. Chem. Soc.* 2010, **132**, 9383.
129. H. Hyunjoo, V. Valerie and N. M. Mathew *J. Phys. Chem. C* 2012, **116**, 22996.
130. M. Li, S. K. Cushing, Q. Wang, X. Shi, L. A. Hornak, Z. Hong, and N. Wu, *J. Phys. Chem. Lett.* 2011, **2**, 2125.
131. M. Kondon, J. Kim, N. Udawatte, D. Lee, *J. Phys. Chem. C* 2008, **112**, 6695.
132. M. Bruchez, M. Moronne, P. Gin, S. Weiss, A. P. Alivisatos, *Science* 1998, **281**, 2013.
133. I. L. Medintz; A. R. Clapp, F. M. Brunel, T. Tiefenbrunn, H. T. Uyeda, E. L. Chang, J. R. Deschamps, P. E. Dawson, H. Mattoussi, *Nat Mater*, 2006, **5**, 581.
134. M. Li, Q. Wang, X. Shi, L. A. Hornak, and N. Wu, *Anal. Chem.*, 2011, **83**, 7061–7065.
135. M. H. Stewart, A. L. Huston, A. M. Scott, A. L. Efros, J. S. Melinge, B. G. Kelly, A. T. Scott, B. B. C. Juan, P. E. Dawson, and I. L. Medintz, *ACS Nano* 2012, **6**, 5330.
136. P. P. Jha and P. Guyot-Sionnest, *ACS Nano*, 2009, **3**, 1011.
137. M. V. Rotello, *ACS Nano*, 2008, **2**, 4.
138. R. Freeman and I. Willner, *Chem. Soc. Rev.* 2012, **41**, 4067-4085
139. A. J. Nozik, M. C. Beard, J. M. Luther, M. Law, R. J. Ellingson and J. C. Johnson, *Chem. Rev.*, 2010, **110**, 6873.
140. P. V. Kamat, K. Tvrdy, D. R. Baker and J. G. Radich, *Chem. Rev.*, 2010, **110**, 6664.
141. A. M. Smith and S. Nie, *Acc. Chem. Res.*, 2010, **43**, 190.
142. M. J. Fernée, P. Tamarat and B. Lounis, *Chem. Soc. Rev.* 2014, **43**, 1311
143. M. J. Polking, H. Zheng, R. Ramesh and A. P. Alivisatos *J. Am. Chem. Soc.*, 2011, **133**, 2044.
144. J. H. Engel, Y. Surendranath, and A. P. Alivisatos, *J. Am. Chem. Soc.*, **2012**, *134*, 13200.
145. S. Kim, S. Hyuk and S.-W. Kim, *Nanoscale*, 2013, **5**, 5205-5214
146. J. Zhang, Y. Fu, M. H. Chowdhury, J. R. Lakowicz, *J. Phys. Chem. C* 2007, **111**, 11784.
147. Z. Chen, S. Berciaud, C. Nuckolls, T. F. Heinz, L. E. Brus, *ACS Nano* 2010, **4**, 2964.
148. A. Kasry, A. A. Ardakani, G. S. Tulevski, B. Menges, M. Copel and L. Vyklicky, *J. Phys. Chem. C*, 2012, **116**, 2858.
149. R. S. Swathi, K. L. Sebastian, *J. Chem. Phys.* 2008, **129**, 054703-1.
150. R. S. Swathi, K. L. Sebastian, *J. Chem. Phys.* 2009, **130**, 086101-1.
151. A. Kim, L. J. Cote, F. Kim and J. Huang, *J. Am. Chem. Soc.*, 2010, **132**, 260.
152. H. Chang, L. Tang, Y. Wang, J. Jiang and J. Li, *Anal. Chem.*, 2010, **82**, 2341.
153. V. Georgakilas, M. Otyepka, A. B. Bourlinos, V. Chandra, N. K. Kim, C. Kemp, P. Hobza, R. Zboril, and K. S. Kim, *Chem. Rev.*, 2012, **112**, 6156.
154. Y. Wang, Z. Li, D. Hu, C.-T. Lin, J. Li and Y. Lin, *J. Am. Chem. Soc.*, 2010, **132**, 9274.
155. J. P. Huang and J. Liu, *Small*, 2012, **8**, 977
156. Y. Liu, X. Dong and P. Chen, *Chem. Soc. Rev.* 2012, **41**, 2283-230
157. Z. Fan, R. Kanchanapally and P. C. Ray, *J. Phys. Chem. Lett.* 2013, **4**, 3813–3818
158. H. Dong, J. Zhang, H. Ju, H. Lu, S. Wang, S. Jin, K. Hao, H. Du and X. Zhang, *Anal. Chem.*, **2012**, *84*, 4587.
159. M. Liu, H. Zhao, X. Quan, S. Chen and X. Fan, *Chem. Comm.*, 2010, **46**, 7909-7911
160. S. Bi, T. Zhao and B. Luo, *Chem. Comm.*, 2012, **48**, 106-108
161. J. A. Dieringer, A. D. McFarland, N. C.; Shah, D. A. Stuart, V. A. Whitney, C. R. Yonzon, M. A. Young, X. Zhang, X.; Van Duyne, R. P. *Faraday Discuss.* 2005 **132**, 926.
162. W. Wei, S. Li, J. E. Millstone, M. J. Banholzer, X. Chen, X. Xu, G. C. Schatz and C. A. Mirkin, *Angew. Chem. Int. Ed.* **2009**, *48*, 4210.
163. S. Lal, N. K. Grady, G. P. Goodrich and N. J. Halas, *Nano Lett.*, 2006, **6**, 2338.
164. A. K. Singh, S. A. Khan, Z. Fan, T. Demeritte, D. Senapati, R. Kanchanapally and P. C. Ray, *J. Am. Chem. Soc.*, 2012, **134**, 8662.

165. B. J. Kennedy, S. Spaeth, M. Dickey, K. T. Carron, *J. Phys. Chem. B* 1999, **103**, 3640.
166. L. Guerrini and D. Graham, *Chem. Soc. Rev.* 2012, **41**, 7085-7107
167. K. A. Willets, *Chem. Soc. Rev.* 2014, DOI: 10.1039/C3CS60334B
168. A. J. Bonham, G. Braun, I. Pavel, M. Moskovits, and N. Reich, *J. Am. Chem. Soc.*, 2007, **129**, 14572.
169. M. Moskovits, *Rev. Mod. Phys.* 1985, **57**, 783.
170. X. Deng, G. B. Braun, S. Liu, P. F. Sciortino, B. Koefler, T. Tomblor and M. Moskovits, *Nano Lett.*, 2010, **10**, 1780.
171. S. M. Ansar, X. Li, S. Zou, and D. Zhang, *J. Phys. Chem. Lett.*, 2012, **3**, 560.
172. E. J. Titus, M. L. Weber, S. M. Stranahan, and K. A. Willets, *Nan Lett.*, 2012, **12**, 5103.
173. D. Drescher and J. Kneipp, *Chem. Soc. Rev.* 2012, **41**, 5780-5799
174. A. Musumeci, D. Gosztola, T. Schiller, N. M. Dimitrijevic, V. Mujica, D. Martin and T. Rajh, *J. Am. Chem. Soc.*, 2009, **131**, 6040.
175. H. Wei and H. Xu, *Nanoscale*, 2013, **5**, 10794-10805
176. S. L. Kleinman, E. Ringe, N. Valley, K. L. Wustholz, E. Phillips, K. A. Scheidt, G. C. Schatz and R. P. Van Duyne, *J. Am. Chem. Soc.*, 2011, **133**, 4115.
177. K. Saha, S. S. Agasti, C. Kim, X. Li, and V. M. Rotello, *Chem. Rev.*, 2012, **112**, 2739.
178. G. Haran, *Acc. Chem. Res.*, 2010, **43**, 1135.
179. L. Brus, *Acc. Chem. Res.*, 2008, **41**, 1742.
180. P. C. Ray, *Chem. Rev.*, 2010, **110**, 5332.
181. B. Yan, Y. Hong, T. Chen and B. M. Reinhard, *Nanoscale*, 2012, **4**, 3917-3925
182. F. Casadio, M. Leona, J. R. Lombardi and R. P. Van Duyne, *Acc. Chem. Res.*, 2010, **43**, 782.
183. K. Kneipp, H. Kneipp and J. Kneipp, *Acc. Chem. Res.*, 2006, **39**, 443.
184. X. Liu, Q. Dai, L. Austin, J. Coutts, G. Knowles, J. Zou, H. Chen, Q. Huo, *J. Am. Chem. Soc.*, 2008, **130**, 2780.
185. S. S. Agasti, A. Chompoosor, Y. Chang-Cheng, S. P. Ghosh, C. K. Kim, V. M. Rotello *J. Am. Chem. Soc.* 2009, **131**, 5728.
186. M. M. Harper, K. S. McKeating and K. Faulds, *Phys. Chem. Chem. Phys.* 2013, **15**, 5312-5318.
187. Y. F. Huang, H. Liu, X. Xiong, Y. Chen and W. Tan, *J. Am. Chem. Soc.*, 2009, **131**, 17328.
188. X. Qian, X. Zhou and S. Nie, *J. Am. Chem. Soc.*, 2008, **130**, 14934.
189. S. Lal, J. H. Hafner, N. J. Halas, S. Link and P. Nordlander, *Acc. Chem. Res.*, 2012, **45**, 1887.
190. E. C. Dreaden and M. A. El-Sayed M. A., *Acc. Chem. Res.*, 2012, **45**, 1854.
191. D. Craig, J. Simpson, K. Faulds and D. Graham, *Chem. Comm.* 2013, **49**, 30-32.
192. S. D. Brown, P. Nativo, J. A. Smith, D. Stirling, P. R. Edwards, B. Venugopal, D. J. Flint, J. A. Plumb, D. Graham and N. J. Wheate, *J. Am. Chem. Soc.*, 2010, **132**, 4678.
193. P. D. Howes, S. Rana and M. M. Stevens, *Chem. Soc. Rev.* 2014, DOI: 10.1039/C3CS60346F
194. S. S. R. Dasary, A. K. Singh, D. Senapati, H. Yu and P. C. Ray, *J. Am. Chem. Soc.* 2009, **131**, 13806.
195. M. A. Berg, R. S. Coleman, C. J. Murphy, *Phys Chem Chem Phys* 2008, **10**, 1229.
196. H. J. Yu, D. Javier, M. A. Yaseen, N. Nitin, R. Richards-Kortum, B. Anvari and M. S. Wong, *J. Am. Chem. Soc.*, 2010, **132**, 1929.
197. S. M. Morton and L. Jensen, *J. Am. Chem. Soc.*, 2009, **131**, 4090.
198. M. M. Maitani, A. A. Douglas, Z. Li, D. L. Allara, D. R. Stewart and S. R. Williams, *J. Am. Chem. Soc.*, 2009, **131**, 6310.
199. W. H. Park and Z. H. Kim, *Nano Lett.*, 2010, **10**, 4040.
200. R. M. Clegg, A. I. H. Murchie, A. Zechel, D. M. J. Lilley, *Proc. Natl. Acad. Sci.* 1993, **90**, 2994.
201. P. J. Hagerman, *Annu. Rev. Biophys. Biol.* 1988, **17**, 265.
202. J. Gersten, A. J. Nitzan, *Chem. Phys.* 1980, **73**, 3023.
203. E. Z. Goude, P. T. Leung, *Solid State Communications* 2007, **143**, 416.
204. Y. D. Yin, L. Gao, and C. W. Qiu, *J. Phys. Chem. C*, 2011, **115**, 8893.
205. R. Rojas, F. Claro, R. Fuchs, *Phys. Rev. B* 1988, **37**, 6799.
206. R. Chang, P. T. Leung, *Phys. Rev. B* 2006, **73**, 125478.
207. H. Y. Chung, P. T. Leung, and D. P. Tsai, *J. Chem. Phys.*, 2013, **138**, 224101.
208. S. Wang, A. K. Singh, D. Senapati, A. Neely, H. Yu and P. C. Ray, *Chem. A Eur. J.*, 2010, **16**, 5600.
209. P. C. Ray, S. A. Khan, A. K. Singh, D. Senapati and Z. Fan, *Chem. Soc. Rev.* 2012, **41**, 3193-3209.
210. Z. Fan, D. Senapati, S. A. Khan, A. K. Singh, A. Hamme, B. Yust, D. Sardar, and P. C. Ray, *Chem. A Eur. J.*, 2013, **19**, 2839-2847
211. W. Lu, A. K. Singh, S. A. Khan, D. Senapati, H. Yu and P. C. Ray, *J. Am. Chem. Soc.*, 2010, **132**, 18103.
212. Z. Fan, M. Shelton, A. K. Singh, D. Senapati, S. A. Khan, and P. C. Ray, *ACS Nano*, 2012, **6**, 1075-1083.
213. S. A. Khan, A. K. Singh, Z. Fan, D. Senapati, P. C. Ray, *Chem Commun.*, 2012, **48**, 11091.
214. A. Huschka, O. Neumann, A. Barhoumi and N. J. Halas, *Nano Letters*, 2010, **10**, 4117.
215. Bakhtiari AB, Hsiao D, Jin G, Gates, BD, Branda NR, *Angew Chem Int Ed Eng.* 2009, **48**, 4166.
216. L. Poon, W. Zandberg, D. Hsiao, Z. Erno, D. Sen, B. D. Gates, and N. R. Branda, *ACS Nano* 2010, **4**, 6395.
217. E. C. Dreaden, A. M. Alkilany, X. Huang, C. J. Murphy and M. A. El-Sayed, *Chem. Soc. Rev.* 2012, **41**, 2740-2779.
218. X. Huang, I. H. El-Sayed, W. Qian, M. A. El-Sayed, *J. Am. Chem. Soc.* 2006, **128**, 2115.
219. Javier D J, Nitin N, Levy M, Ellington A and Richards-Kortum R, *Bioconjugate Chem.*, 2008, **19**, 1309.
220. G. Sardana, K. Jung, C. Stephan and E. P. Diamandis, *J. Proteome Res.*, 2008, **7**, 3329.
221. W. Lu, S. A. Arumugam, D. Senapati, A. K. Singh, T. Arbnesi, S. A. Khan, H. Yu and P. C. Ray, *ACS Nano*, 2010, **4**, 1739.
222. H. J. Yu, D. Javier, M. A. Yaseen, N. Nitin, R. Richards-Kortum, B. Anvari and M. S. Wong, *J. Am. Chem. Soc.*, 2010, **132**, 1929.
223. A. Wijaya, S. B. Schaffer, I. G. Pallares and K. Hamad-Schifferli, *ACS Nano*, 2009, **3**, 80.
224. S. S. Agasti, A. Chompoosor, Y. Chang-Cheng, P. Ghosh, C. K. Kim, V. M. Rotello *J. Am. Chem. Soc.* 2009, **131**, 5728.
225. A. Nel, T. Xia, H. Meng, X. Wang, S. Lin, Z. Ji, and H. Zhang, *Acc. Chem. Res.*, 2013, **46**, 607-621.
226. S. Sharifi, S. Behzadi, S. Laurent, M. L. Forrest, P. Stroeve and M. Mahmoudi, *Chem. Soc. Rev.* 2012, **41**, 2323-2343.
227. F. M. Winnik and D. Maysinger, *Acc. Chem. Res.*, 2013, **46**, 672.
228. C. Chen, Y.-F. Li, Y. Qu, Z. Chai and Y. Zhao, *Chem. Soc. Rev.* 2013, **42**, 8266-8303.
229. G. E. Batley, J. K. Kirby, and M. J. McLaughlin, *Acc. Chem. Res.*, 2013, **46**, 854-862.
230. F. Joris, B. B. Manshian, K. Peynshaert, S. C. De Smedt, K. Braeckmans and S. J. Soenen, *Chem. Soc. Rev.* 2013, **42**, 8339-8359.
231. A. M. Alkilany, S. E. Lohse, and C. J. Murphy, *Acc. Chem. Res.*, 2013, **46**, 650-661.
232. S. T. Kim, K. Saha, C. Kim, and V. M. Rotello, *Acc. Chem. Res.*, 2013, **46**, 681-691.

#### 14. Table of Content Figure

